Búsquedas de partículas de larga vida en CMS

(Searches for long-lived particles at CMS)

Trabajo de Fin de Máster
para acceder al

MÁSTER EN FÍSICA DE PARTÍCULAS Y DEL COSMOS

Autor: Yimi Josue Perla Rosa

Director: Jesús Manuel Vizán García

julio - 2021

ABSTRACT

Long-lived particles appear as predictions in many beyond the Standard Model theories. In this work a hypothetical process is explored in which a non-Standard Model Higgs boson produces a pair of long-lived spinless X bosons, each of which produces a dilepton. This is based on an ongoing analysis at CMS using proton-proton collisions at a 13 TeV centre of mass energy.
The main objective is to study optimal cuts related to the flight distance and impact parameter of the long-lived particles. First, the distribution of displacement and kinematics for a set of different signals are examined at generation level, to have a ground of comparison to the next part in which reconstruction is approached for the flight distance L_{xy} , flight distance to error ratio I_{xy} , impact parameter d_{xy} and impact parameter to error ratio $d_{xy}/\sigma(d_{xy})$. The signal significance was calculated for the reconstructed cases, finding distinct behaviors for different signals. On this basis, some regions for optimal cuts are singled out. Finally, a comparison between flight distance and impact parameter at generation level is shown, also finding distinct results for different signals.

Keywords: Long-Lived Particles, CMS experiment, LHC, High-energy physics, Beyond Standard Model, Data Analysis, Higgs.

Resumen

Las partículas de larga vida aparecen como predicciones en las teorías más allá del Modelo Estándar. En este trabajo, se explora un hipotético proceso en el cual un bosón de Higgs no perteneciente al Modelo Estándar, produce un par de bosones X de espín nulo y de larga vida, cada uno de los cuales produce luego un dileptón. El presente se basa en un análisis en marcha del CMS que usa colisiones protón-protón a una energía de centro de masa de 13 TeV.
El objetivo principal es estudiar cortes óptimos relacionados con la distancia de vuelo y el parámetro de impacto de las partículas de larga vida. Primero, la distribución del desplazamiento y la cinemática para un conjunto de señales son examinados a nivel de generación, esto para tener un punto de comparación con la siguiente parte en la cual se aborda la reconstrucción para el parámetro de vuelo L_{xy} , la razón del parámetro de vuelo a su error I_{xy} , el parámetro de impacto d_{xy} y la razón del parámetro de impacto a su error $d_{xy}/\sigma(d_{xy})$. La significancia de señal fue calculada para los casos reconstruidos, encontrando distintos comportamientos para las diferentes señales, en base a esto, algunas regiones para cortes óptimos fueron señaladas. Finalmente, se muestra una comparación entre la distancia de vuelo y el impacto de parámetro a nivel de generación, encontrado también diversos resultados para las distintas señales.

Palabras clave: Partículas de larga vida, experimento CMS, LHC, Física de altas energías, Más allá del Modelo Estándar, Análisis de datos, Higgs.

Contents

List of Tables

List of Figures

1. INTRODUCTION

The physics of particles and their fundamental interactions is well described by the Standard Model (SM) theory, which has been successful at describing experimental observations. The SM started to take form in the 1960s decade through the work of Sheldon Glashow, Steven Weinberg, Abdus Salam and others, taking the Quatum Field Theory (QFT) as a basis to unify weak and electromagnetic interactions, classify the known elementary particles, explain their interactions and provide a mechanism by which mass is obtained. Since its introduction, successive experiments confirmed its predictions through the years, for example the W and Z bosons discovery in 1983 [1], the top quark discovery in 1995 [1] and the Higgs boson discovery in 2012 [2][3]. However, there are still open questions like the nature of dark matter, the low ratio of antimatter to matter in the Universe and the neutrino masses which are not under the scope of the SM, but could be explained by the existence of new particles and interactions not included in it, going to the so called Beyond the Standard Model (BSM) physics.

A motivation behind the search for new Long-Lived Particles (LLP) is because these are predicted in some BSM theories, for example in Supersymmetry (SUSY). Not only a new particle of this type could point to new physics but also the particle itself could be interesting as candidates for dark matter particles, some of which come naturally in certain SUSY models, are being explored. This work will be focused in the search of LLPs in the *Large Hadron Collider* (LHC), particularly in the *Compact Muon Solenoid* (CMS) experiment.

Here a process is explored in which a Higgs boson produces a pair of spinless X bosons and each of these produce either a e^-e^+ or $\mu^-\mu^+$ pair. The present work is based on an ongoing search of LLPs at the *Instituto de Física de Cantabria* using CMS data for proton-proton collisions at a 13 TeV centre of mass energy [4]. No specific model is assumed in this search, and different possibilities for mass and mean lifetime are considered for the sought particles. Since this would lead to different behavior in the signals, variables related to the kinematics and flight distance of the particles will be first studied at generation level using Monte Carlo simulated samples. Then the reconstruction results for different signals are approached trying to understand the behavior of four variables: flight distance L_{xy} , flight distance to error ratio I_{xy} , impact parameter d_{xy} and impact parameter to error ratio $d_{xy}/\sigma(d_{xy})$ and a figure of merit called *signal significance* will be used to evaluate their performance. Finally, the correlation of L_{xy} and d_{xy} is briefly discussed at generation level, being something that could be used in a future analysis.

In this work, the SM, its limitations, alternative models and the concept of long lived particles are briefly addressed in Chapter 2. The Chapter 3 is dedicated to the LHC and mostly to the CMS detector and its sub-systems that are relevant to this analysis. Chapter 4 approaches both the generalities of data processing and reconstruction in CMS and also particular algorithms and selections used in the search of LLPs. In Chapter 5 the analysis is presented for the process described in the previous paragraph. Finally, in Chapter 6 conclusions are given.

2. THEORY

2.1 Standard Model

The current understanding of particle physics is summarized in the Standard Model theory, in which a set of elementary particles and their interactions are defined, managing to describe experimental observations in a satisfying manner. A summary of the elementary SM particles is shown in table 2.1:

	FERMIONS				BOSONS	
Generation:	I	II	III	Type:	Gauge	Scalar
	Quarks					
Mass: Charge: Spin:	2.16 MeV 2/3 1/2 u up	1.27 GeV 2/3 1/2 c charm	172.76 GeV 2/3 1/2 t top		0 0 1 γ photon	125.10 GeV 0 0 H higgs
	4.67 MeV -1/3 1/2 d down	93 MeV -1/3 1/2 s strange	4.18 Gev -1/3 1/2 b bottom		0 0 1 g gluon	
	Leptons					
	0.511 MeV -1 1/2 e electron	105.7 MeV -1 1/2 μ muon	1777 MeV -1 1/2 τ tau		91.19 GeV 0 1 Z Z boson	
	<1.1 eV 0 1/2 νe electron neutrino	<190 keV 0 1/2 νμ muon neutrino	<18.2 MeV 0 1/2 ντ tau neturino		80.38 GeV ±1 1 W W boson	

Table 2.1: Elementary particles of the Standard Model of particle physics [5].

According to their spin, particles can be classified as fermions and bosons. Fermions have half-integral spin and follow Fermi-Dirac statisitcs, leptons and quarks as seen in table 2.1 have spin ½. Bosons, on the other hand, are integer spin particles and follow Bose-Einstein statistics, for example, protons which are composite particles, are bosons with spin 1.

The twelve fundamental fermions in the SM are divided in six quarks and six leptons, all of these come in three generations. Most of the matter with which we interact can be described by the first generation as quarks up and down are in the internal structure of neutrons and protons, these together with electrons constitute atoms. The generations II and III particles are like the first generation ones but more massive. Neutrons, which at some point where thought to be massless are now known to have some small albeit non-zero mass [6], with a value yet to be determined but with an upper limit progressively decreasing through experiments.

In physics, four fundamental forces are known: electromagnetic, weak, strong and gravitational, with associated bosons to them, as seen in table 2.2. Gravitational force is out of the scope of SM.

Interaction	Boson	Spin	Existence
Electromagnetic	Photon	1	Confirmed
Weak	W and Z	1	Confirmed
Strong	Gluon	1	Confirmed
Gravitational	Graviton	2	Unconfirmed

Table 2.2: Gauge bosons.

On the other hand, the Higgs boson, a spin zero scalar boson, is the particle associated to the Higgs mechanism by which particles acquire mass [7]. At high energies, electromagnetic and weak

interactions have the same intensity and element particles are massless, when the energy is lowered, there is a point in which this symmetry is spontaneously broken and W bosons together with the Z bosons acquire masses through the Higgs field. Then at lower temperatures the electromagnetic and weak interaction have different intensity because the interaction particle of the former -the photon- is masless whereas the W and Z associated with the later have mass. Fermions can also acquire mass through interaction with the Higgs field.

In SM, interaction between particles occurs through the exchange of these bosons. For example, two particles with positive electrical charge repel each other by exchanging photons which are the gauge bosons of the electromagnetic interaction, in this case, the reaction is not instantaneous as the SM is build taking Special Relativity (SR) into account, thus all interaction happen with the speed of light as a speed limit. The fundamental forces do not necessarily act over all matter, only gravitation does, so the Strong force acts on quarks and not on leptons because the former have color charge and the later do not. Relative strength greatly differs, as at low energies the Strong interaction is 10^{38} times stronger than the gravitational interaction. A summary of the fundamental forces is given in table 2.3:

Force	Relative strength	Exchange particle (bosons)	Particles acted upon	Range
Strong	1	Gluon	Quarks	10^{-15} m
Electromagnetic	1/137	photon	Charged particles	∞
Weak	10^{-10}	W^+, W^-, Z bosons	Quarks, leptons, neutrinos	10^{-18} m
Gravitational	10^{-38}	graviton	All particles	∞

Table 2.3: Fundamental forces. From Ling, Sanny, Moebs [8].

The SM is built over QFT as a gauge theory, that is, based on symmetries. It is particularly based in the local group of symmetries $SU(3)_c \otimes SU(2)_L \otimes U(1)_Y$ where subscript c stands for color, L for left chirality and Y is hypercharge. $SU(3)_c$ describes the Quantum Chromodynamics, i.e. the strong interaction and $SU(2)_L \otimes U(1)_Y$ accounts for the electroweak interaction symmetry.

2.1.1 The Higgs boson

The Higgs mechanism, associated to the Higgs boson is the process by which the W and Z bosons acquire mass. This mechanism comes from the breaking of the $SU(2)_L \otimes U(1)_Y$ local gauge electroweak symmetry of the Standard Model. The idea is that a complex scalar field ϕ associated with a SM lagrangian can be written so its minimum is at zero as in figure 2.1.a, or with a minimum not in zero but around it like in figure 2.1.b.

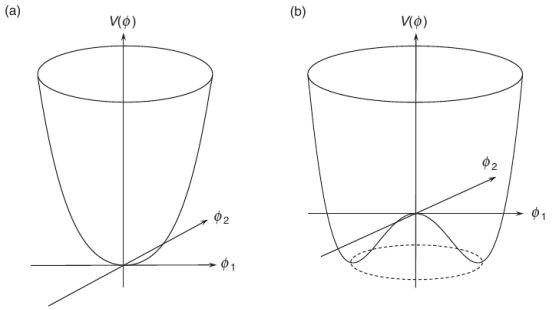

Figure 2.1: Potential for a complex scalar field. a) Minimum at one point, in this case zero. b) The minimum is in a circle around zero. From Thomson [9].

The first is a not so interesting case with a potential in a single point, but for the second one, the minimum can be any point over a circle and by choosing one, we have symmetry breaking. Particles associated with excitations of the scalar field in the direction of unchanging potential in this minimum are referred in general as "*Goldstone bosons*" [9].

Taking this idea further to the electroweak symmetry, and breaking it, we get Goldstone bosons that could absorbed into components of the Z and W bosons giving them their masses. The Lagrange corresponding to the used potential can be written in a way that manifests a massive scalar Higgs field associated to the Higgs boson. The Higgs field permeates all space. At high energies, it does not manifest spontaneous symmetry breaking and the Z, W bosons are massless.

2.2 Beyond the Standard Model

2.2.1 Unanswered questions by the Standard Model

There are open questions beyond the scope of the Standard Model that could be answered by a more complete particle physics theory, some being:

- Nature of Dark Matter: General Relativity is a theory which successfully establishes a relationship between gravity and mass. However, galaxy observations show gravitational effects that points to a greater mass content than what is observed [10]. This could be explained by the existence of a hypothetical form of matter which interacts weakly with ordinary (baryonic) matter, known as Dark Matter but no particle in the Standard Model could be attributed to it in a satisfactory way. Neutrinos, which also interact weakly with baryonic matter where once proposed as the components of Dark matter, but this idea has been abandoned [11]. Dark Matter would be composed of one (or more than one) yet to be observed particle.

- Low ratio of antimatter to matter in the Universe: Each particle in the Standard Model has an antiparticle, differing only in electric charge. A particle with neutral electric charge as the photon is its own antiparticle. If a particle encounters its antiparticle, they would annihilate each other. Matter made out of antiparticles is known as antimatter but their physical behavior is the same. Our Universe is made almost entirely of matter [12] and the SM is unable to explain why it prevails over antimatter, this is known a the matter-antimatter asymmetry problem.

- Neutrino masses: Neutrinos where originally conceived as massless in the SM [13], but later experiments have shown the existence of neutrino oscillation by which neutrinos can change their flavor[14]. This implies neutrino masses are not zero. These particles would have a much lower mass than their associated charged lepton, with current upper limits given by beta decay shown in table 2.1. The discovery of neutrino oscillations is the first experimental result indicating physics beyond the SM. The actual mechanism by which neutrinos acquire such a low mass is not known.

- Hierarchy problem: SM does not explain why the gravitational interaction is many orders of magnitude weaker than weak interaction. Given this difference, under the SM, the Higgs boson mass would be expected to be in the Planck mass scale at 10^{19} GeV [15], but it was experimentaly found to be in the 10^{2} GeV order of magnitude [2][3], which is closer to the electroweak scale. This would require a very unnatural fine tunning for the Higgs boson to be so small.

2.2.2 Proposed theories

Some BSM theories are:

- Supersymmetry (SUSY): This theory postulates that each particle in the SM has a superpartner whose spin differs in one half, that is, each fermion has a boson superpartner and each boson has a fermion superpartner. SUSY could solve the hierarchy problem, lead to gauge coupling unification and potentially provide a dark matter particle candidate. These additional particles are the key to cancel quadratically divergent mass terms of all orders that leads to the hierarchy problem.

SUSY is not a single model, as there exists several variations of it, in many of these models, supepartners can decay until producing the Lightest Supersymmetry Particle (LSP) which is to be stable and neutral. This particle would be abundant in the Universe and weakly interacting with ordinary matter, thus becoming a theoretical candidate for a dark matter particle [16].

One model is the Minimal Supersymmetric Standard Model (MSSM) which is a extension of the SM that introduces supersymmetry while using the lowest number of particles and interactions without breaking compatibility with known physics [17]. To enforce lepton and baryon number conservation, the MSSM imposes a symmetry called R-Parity that comes as a discrete quantity that takes a value +1 for SM particles and -1 for their superpartners.

As of date, the new particles predicted by SUSY have not been experimentally found, although there are active searches for them, particularly in the LHC. But this has lead to go beyond simple SUSY models like MSSM [18], one example would be the extension called R-Parity Violating Supersymmetry (RPV SUSY) in which, as its name implies, is possible to violate the R-Parity supersimmetry through sufficiently small couplings in the operators, this theoretically leads to long-lived SUSY particles.

- Extra dimensions: The Standard Model is a four-dimensional theory, with three being spatial and one temporal. Extra-dimensional theories propose the existence of more dimensions which are mostly inaccessible being extremely hard if not impossible to experimentally proof. These theories aim to answer in a fundamental way, questions the SM is not able to. For example, the “Large Extra Dimensions” model approaches the hierarchy problem by suggesting that the universe exists in a 11 dimensional membrane, the electromagnetic, weak and strong force would act on four of its dimensions, while the gravitational force acts on the eleven dimensions, thus giving the appearance of being weaker than the rest of forces to an observer able to only perceive four dimensions. These kind of theories are not incompatible with SUSY, for example the “Superstring theory” is constructed using it as a basis.

2.2.3 Long lived particles

Some of the SM fundamental particles and many composed ones are unstable, but with varying mean lifetimes. For example, the tau has a mean life of 0.29 picoseconds, on the other hand, the muon is much more long lived at 2.2 microseconds. There are BSM theories which propose the existence of additional Long Lived Particles (LLP) that could live for some nanoseconds and have observable decays in periods when no LHC collisions are taking place [19]. Some of these theories are: mini split SUSY, gauge-mediated SUSY breaking, R-parity violating SUSY, Stealth SUSY, Neutral Naturalness models, Hidden Valley models, etc [20]. In figure 2.2 the lifetimes for some particles is shown.

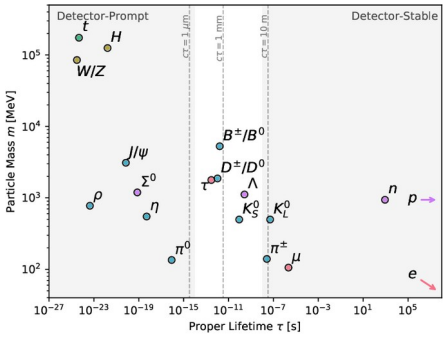

Figure 2.2: Mass versus Proper Lifetime for some particles in the Standard Model. From (Lee et al. 2019 [21]).

Here, a model is explored in which the Higgs boson decays into a pair of long-lived, spinless X bosons. Then a X boson is able to decay into SM dileptons as in figure 2.3. These leptons would be observed in the detector.

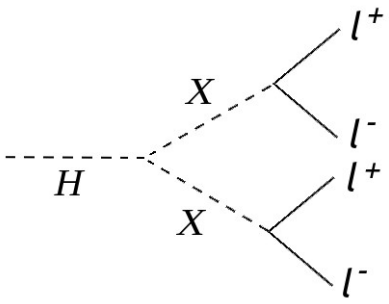

Figure 2.3: X boson production from Higgs boson, and then decay into dileptons.

3. EXPERIMENT DESCRIPTION

The experimental data is taken from the Run 2 of the Large Hadron Collider (LHC), collected in the Compact Muon Solenoid (CMS). This experimental run is characterized by a centre-of-mass energy of 13 TeV and samples correspond to a 35.87 fb^{-1} integrated luminosity. In this section, the LHC and the CMS detector will be described.

3.1 Large Hadron Collider

The LHC is a circular particle accelerator, built by the European Organization for Nuclear Research (CERN). It consists of a 27 kilometer ring of superconducting magnets and accelerating structures. Inside the accelerator, two particle beams -consisting of either protons or ions- are accelerated in opposite directions, approaching the speed of light before colliding [22].

The idea behind the construction of the LHC was gestated in the 1980s as option to follow the previous Large Electron-Positron Collider (LEP) by taking advantage of the tunnel built for it, this was in consideration even before the LEP started operation in 1989. The project was approved by the CERN council in 1994. Eventually, ATLAS (A Toroidal LHC Apparatus, CMS (Compact Muon Solenoid), LHCb (LHC-beauty) an ALICE (A Large Ion Collider Experiment) where the first experiments to receive approbation and to begin to be constructed in different sites of the tunnel. The LHC started operations September 10 of 2008, but an electrical fault that caused extended damage, delayed the first collisions until November 2009 when the LHC re-started [23]. Due to technical problems, the energy was limited to 1.18 TeV in 2009. The first long running period of the LHC started on February 2010 at a beam energy of 3.5 TeV [24]. The operation from its restart in 2009 to Febrary 16 of 2013 it's known as the Run 1 of the LHC. This first run saw major advances in particle physics, including the discovery of a new boson consistent with the predicted Higgs boson. A simple scheme of the LHC is shown in figure 3.1.

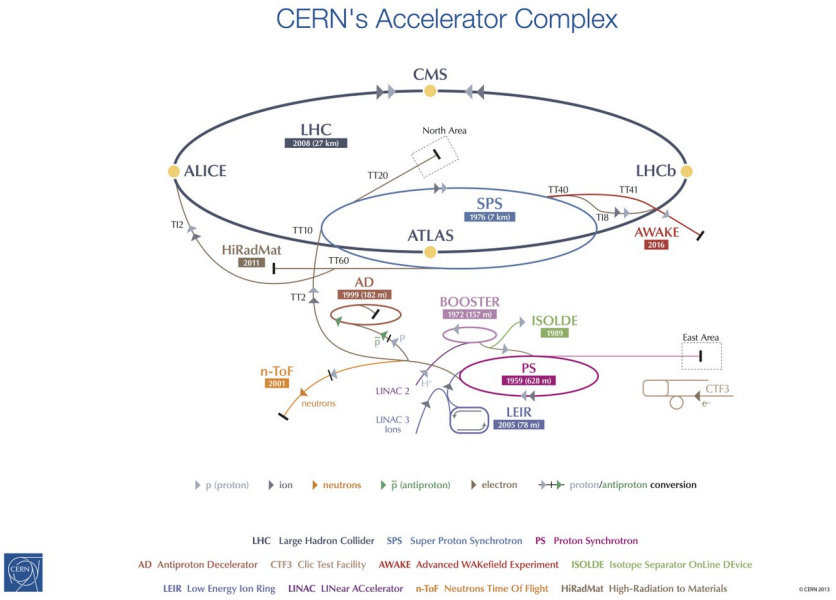

Figure 3.1: Schematic representation of the CERN accelerator complex. From CERN [25].

The Run 2 of the LHC went on from 2015 to 2018, reaching a centre-of-mass energy of 13 TeV. Details of this run are given on the table 3.1:

Quantity	Number
Circumference	26 659 m
Dipole operating temperature	1.9 K (-271.3°C)
Number of magnets	9593
Number of main dipoles	1232
Number of main quadrupoles	392
Number of RF cavities	8 per beam
Nominal energy, protons	6.5 TeV
Nominal energy, ions	2.56 TeV/u (energy per nucleon)
Nominal energy, protons collisions	13 TeV
No. of bunches per proton beam	2808
No. of protons per bunch (at start)	1.2×10^{11}
Number of turns per second	11245
Number of collisions per second	1 billion

Table 3.1: Figures for the Run 2 of the LHC. From CERN [25].

A Run 3 is planned to start in 2022 with increased energy [26]. A comparison of parameters for different runs is shown in table 3.2:

Parameter	Design	Run-1	Run-2	Run-3	HL-LHC
Energy [TeV]	14	7/8	13	14	14
Bunch spacing [ns]	25	50	25	25	25
Bunch Intensity [10^{11} ppb]	1.15	1.6	1.2	up to 1.8	2.2
Number of bunches	2800	1400	2500	2800	2800
Emittance [μm]	3.5	2.2	2.2	2.5	2.5
β^* [cm]	55	80	$30 \rightarrow 25$	$30 \rightarrow 25$	down to 15
Crossing angle [μrad]	285	-	$300 \rightarrow 260$	$300 \rightarrow 260$	TBD
Peak Luminosity [10^{34} cm^{-2}s^{-1}]	1.0	0.8	2.0	2.0	5.0
Peak pileup	25	45	60	55	150

Table 3.2: Comparison of figures for different running periods of the LHC. From Boyd [27].

The LHC operation starts on the LINAC 2 linear accelerator, here protons are extracted from a bottle of Hydrogen gas, accelerating a beam to 50 MeV over a distance of 33 m. Particles then proceed to the Proton Synchrotron Booster (PSB), reaching a energy of 1.4 GeV in 1.2 s, after that, they go to the Proton Synchrotron further increasing their energy to 26 GeV. After that, protons are injected into the Super Protron Synchrotron (SPS), increasing again their energy to 450 GeV. Finally, protons go to the LHC main ring, in two beams circulating in opposite directions, reaching in the Run 2 a centre-of-mass energy of 13 TeV before colliding [28].

3.2 Compact Muon Solenoid

The CMS is a general-purpose detector installed at the LHC. It is built around a solenoid magnet capable of generating a magnetic field of 4 tesla. The detector measures 21 meters long, 15 meters wide and 15 meters high, it has a weight of 14,000 tons [29].

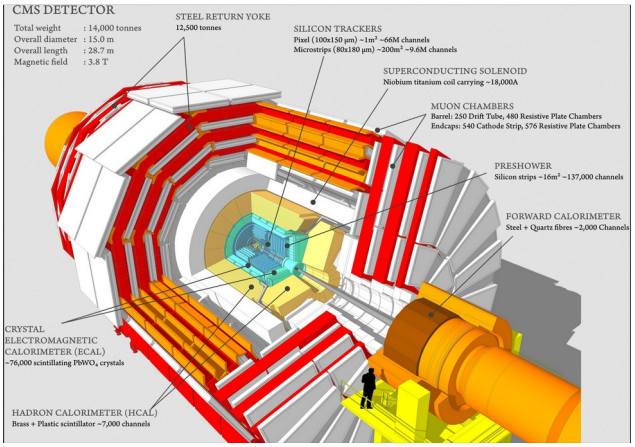

Figure 3.2: Schematic view of the CMS. From CERN [30].

The detector is located in one of the points where the accelerated beams of the LHC are made to collide, then the resulting particles are studied using the sub-detector devices installed in CMS. Unstable particles produced in these collisions are not directly observed, however by studying stable and highly interacting particles such as electrons and muons, it is possible to find out what else was produced; for example, the neutrinos are weakly interacting with the ordinary matter and can easily transverse all the CMS without triggering any signals, but an analysis of the detected particles can show an energy deficit which could be associated with neutrino production.

A magnetic field of 4 tesla is generated by the solenoid, this bends the trajectory of the particle which helps to obtain important information as differently charged particles bend in opposite directions under the magnetic field, also this gives information on the linear momentum for a larger momentum translates in a less bent trajectory. A series of layered concentric silicon trackers are used to reconstruct the trajectory of the particles.

To measure energy, the CMS has installed the Electromagnetic Calorimeter (ECAL) which is able to stop electrons and photons, collecting information on their energy. Hadrons can go through the ECAL but are eventually stopped in an outer layer, the Hadron Calorimeter (HCAL). Muons are not stopped by the calorimeters, but produce hits in special sub-detectors called Muon Detectors beyond the calorimeters. Schemes of the CMS can be seen in figures 3.2 and 3.3

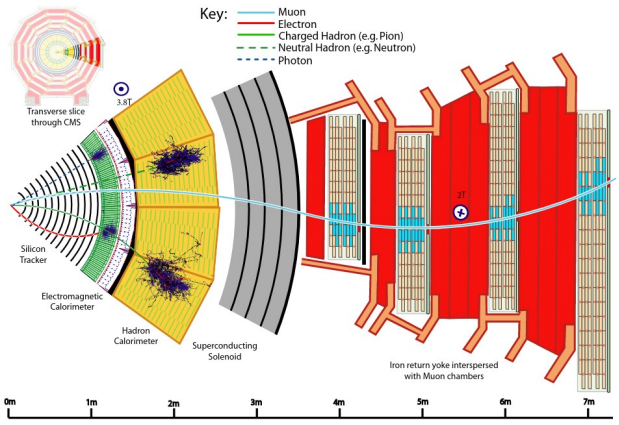

Figure 3.3: Transverse section view of CMS showing particles interactions. From Sirunyan et al. [31].

For reference, a right-handed coordinate system is used in the CMS, with the x axis pointing towards the center of the LHC, the y axis is perpendicular to the LHC plane and points upward, the z axis points in the anticlockwise direction of the beam. The azimuthal angle φ is measured in radians with respect to the x axis in the xy plane, the polar angle θ is measured with respect to the positive z axis. Pseudorapidity η of the particles is defined as $-\ln[\tan(\theta/2)]$ [32][33].

3.2.1 The CMS tracking system

The tracking system is the part that collects data for the latter reconstruction of the particles trajectories. It consists of a inner pixel detector close to the particle beam, surrounded by several layers of silicon strip detectors as seen in figure 3.4.

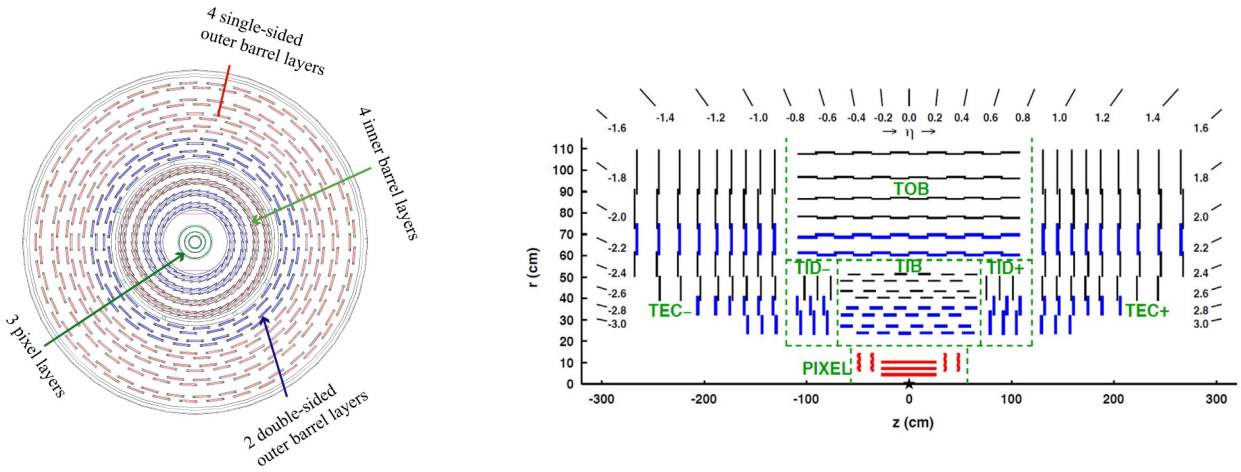

Figure 3.4: Slided section view of the CMS tracker. Left: transverse to the beam axis. From CERN [34]. Right: coplanar with the beam axis. From Viliani [35].

The pixel detector has three barrel pixel (BPIX) layers and two endcap disks at each side, its internal radius is 4 cm and its external radius is 15 cm with a length of 98 cm along the beam [36]. The purpose of this detector is vector finding and flavor tagging, as this requires tracking as close to the beam collision point to be efficient [37].

Next is the silicon strip tracking system, which consists of ten barrel layers with twelve endcap disks at each side. It has 25 cm of internal radius, 110 cm of external radius and 560 cm length along the beam. This part starts with four inner barrel (TIB) layers covered by two inner endcaps composed each by three disks (TID), the first two layers are double sided. After that there is the outer barrel (TOB) consisting of six layers of which the first two are also double sided. Covering this, there are two tracker endcaps (TEC) with nine disks each [36][37]. The double sided layers are composed of two single sided sensors mounted back to back and rotated 100 mrad with respect to each other, their purpose is to provide 3-dimensional tracking data [35].

Silicon sensors are used due to their fast response time and excellent resolution, which is of high importance in this region close to the beam as there is a high number of events. In these, charged particles interact electromagnetically with the material, producing a small current signal, this is known as a hit. The tracker was designed to operate at an instantaneous luminosity of $1.0\times10^{34}cm^{-2}s^{-1}$, an integrated luminosity of $500\,fb^{-1}$ and an average pileup of 20-30 collisions per bunch crossing, its acceptance covers up to a pseudorapidity of $|\eta|\approx2.4$ [38].

3.2.2 Electromagnetic Calorimeter

The main objective of the CMS Electromagnetic Calorimeter is energy measuring of electrons and photons. The ECAL is a high resolution, homogeneous calorimeter composed of 75,848 lead tungstate $(PbWO_4)$ scintillating crystals. It is structured as a barrel (EB) section with 61,200 crystals arranged in 36 supermodules cointaining 1700 crystals each, covering a pseudorapidity region of $|\eta|<1.48$ and covered by two endcaps (EE) with 7324 crystals each, divided in two halves or "Dees", extending the pseudorapidity coverage to a $|\eta|<3$ region [39][40]. A simple scheme of the ECAL can be seen in figure 3.5:

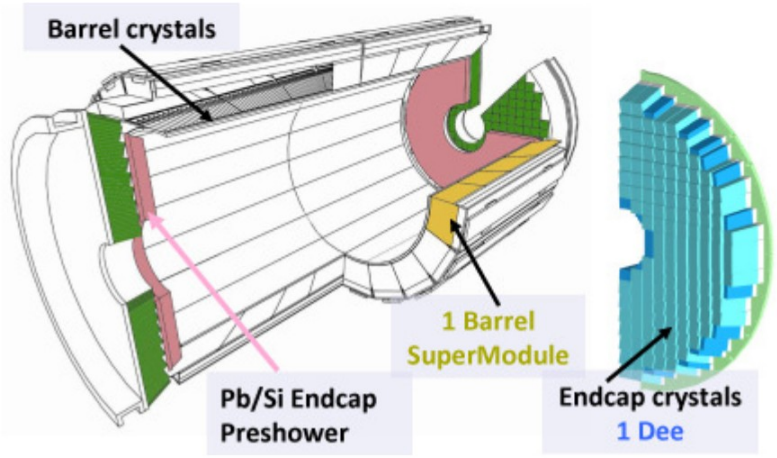

Figure 3.5: Schematic view of the CMS Electromagnetic Calorimeter. From Biino [41].

In the endcap regions there are detectors called Preshower (ES). The function of these is to tell apart single high-energy photons which are interesting from closely spaced pairs of photons produced in neutral pion decays, as the later could mimic the former in their energy signature. These detectors consist of two layers of lead, each followed by silicon strip sensors. There are 4288 sensors covering a pseudorapidity region $1.65<|\eta|<2.6$. An incoming photon produces an electromagnetic shower in the lead, containing electron-positron pairs which are then detected by the silicon strips, the double layer design gives two measurements which allows to track the original photon [41] [42].

In the ECAL, electrons and photons produce scintillation while going through the crystals, that is, light is generated by the passage of these particles. Avalance photodiodes (APD) in the EB section and Vacuum phototriodes (VPT) convert this light in electrical signal, which is sampled every 25 ns to obtain signal waveforms with an amplitude proportional to the energy deposited by the particles [43]. The sampled signals are packed in Trigger Primitives (TP) which are sent to the Level 1 Trigger, these data sets also contain readings from others sub-detectors for later reconstruction of electrons, photons, jets and sums of transverse energy.

3.2.3 Hadron Calorimeter

The Hadronic Calorimeter measures energy of hadrons, and also can provide indirect measurement of neutrinos. Althought this part of the CMS is not relevant to this analysis, here it will be briefly described for completeness and because it could be used in future approaches for background signal reduction, for example, exploring the top-antitop production. The HCAL is divided in four sections: Barrel (HB), Endcap (HE), Outer (HO) and Forward (HF), as seen in figure 3.6.

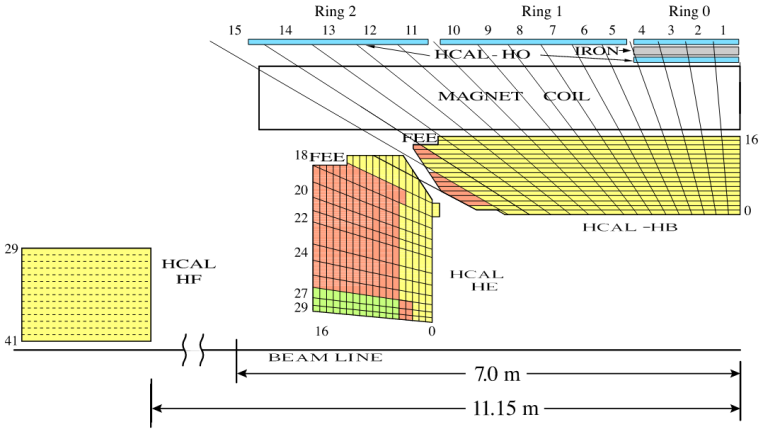

Figure 3.6: Slided (quarter) scheme of the Hadron Calorimeter coplanar with the beam. From the CMS Collaboration [44].

The HB and HE are sampling calorimeters made of alternating layers of brass for absortion and plastic scintillators. These are contained by the solenoid which produces the 4 T magnetic field. There is a gap between both calorimeters as seen in figure 3.6, but is not aligned with the center of the CMS so is not an uncovered region. HB covers the pseudorapidity angle $0<|\eta|<1.4$ and HE covers $1.3<|\eta|<3$, the $1.3<|\eta|<1.4$ range is covered by both [44][45].

The HO is located outside the solenoid and its function is to ensure high energy shower do not escape from the CMS without measurement. It has plastic scintillator material and uses the CMS magnet material, for example the iron return yoke, as absortion layer. The HO calorimeter covers $|\eta|<1.26$ [46].

For the HB, HE and HO the idea is the same; hadronic particles hit an absorber layer producing secondary particles, these continue interacting with the absorbing material generating a shower of particles, going through the alternated scintillation layers these particles produce light which has to be converted to an electric signal, by hybrid photodiodes (HPD) in the case of HB and HE, and by silicon photomultipliers (SiPM) in the case of HO [46]. The signals are digitized and combined, from this the deposited energy by incoming particles can be obtained [47][48].

To cover a higher pseudorapidity, the HF section is installed separatelly, 6 m away from the HE endcap. it covers the region $2.85<|\eta|<5.19$. The HF is a Cherenkov calorimeter using quartz fibers embedded with steel. The fibers, 5 mm spaced, collect the Cherenkov light produced by the shower of particles that is generated by the hadronic particles interacting with the absorbing material. Again, photodetectors collect the light and generate an electrical signal from which the energy deposited can be obtained [45][46].

3.2.4 Superconducting solenoid

With a length of 12.5 m and bore diameter of 6 m, the CMS solenoid produces an uniform central magnetic of 4T in the direction of the beam. This field is important for good resolution in the measurement of muon momentum. The inner bore diameter is large enough to contain the tracker and calorimeters. Outside the solenoid, a 1.5 m thick iron yoke is responsible for the return of the magnetic flux [49][50]. A representation of the solenoid is shown in figure 3.7.

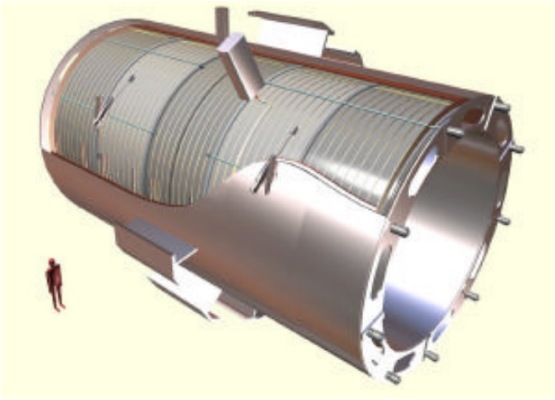

Figure 3.7: Artistic representation of the CMS solenoid. From Kircher et al. [50].

3.2.5 Muon detector system

Beyond the solenoid is the muon detection system, its function is to identify muons and measure their momentum. Assembled in layers of gas-ionization detectors interleaved with the iron yoke, it is enclosed by two endcaps and covers the pseudorapidity region $|\eta|<2.4$. The system uses three different technologies: Drift Tube (DT) chambers, Cathode Strip Chambers (CSC) and Resistive Plate Chambers (RPC) [51], distributed as seen in figure 3.8.

The barrel zone with the iron yoke and Muon detectors is segmented in five wheels, contained in the barrel there are 250 Drift Tubes, covering an pesudorapidity region $|\eta|<1.3$. In this zone the muon rate is relatively low and the magnetic field at an intensity below 0.4 T is almost uniform. Radially, from center to outwards there are four stations; the MB1, MB2 and MB3 stations contain 60 DTs, and the MB4 station contains 70 DTs. These chambers have rectangular cells with a gas mixture of 85% Ar and 15% CO_2, with a anode wire at the center [52]. Here muons produce signals by ionizing the gas, the removed electrons drift towards the positively charged wire. The position of the muon is found by measuring the drifting time of the electrons since the drifting speed is approximately constant.

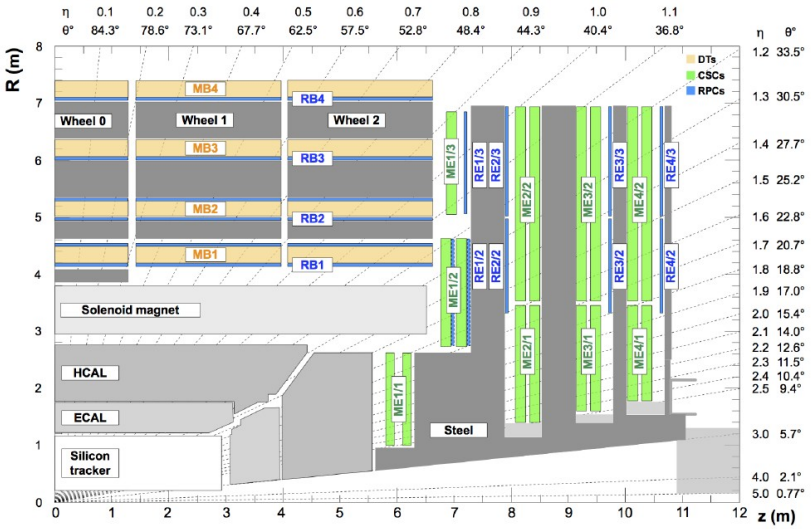

Figure 3.8: Slided (quarter) scheme of the Muon detector system coplanar with the beam. From the CMS Collaboration [53].

Cathode Strip Chambers are found in the endcap regions where the muon rate is relatively high and the magnetic field is intense as well as non uniform. There are 540 CSCs distributed in four stations: ME1, ME2, ME3 and ME4, each chamber module has 6 layers. These detectors are arranged in rings concentric with the beam, the first station has three rings while the others have 2 rings each. A CSC consists of an grid made negatively charged cathode strips and perpendicular to these, positvely charged anode wires, the gas in the chamber is a mixture of 50% CO_2, 40% Ar and 10% CF_4 [52]. CSCs cover the pseudorapidity range $0.9<|\eta|<2.4$. When an incoming muon ionizes one atom of the gas, a ripped out electron goes to the wire while the positive ion goes to the strip, both create en electric current and due to the geometry of the grid, this gives two spatial coordinates to locate the muon. Consecutive detector layers are used to give tracking information.

Resistive Plate Chambers are distributed with 480 chambers in the barrel and 576 chambers in the endcap regions [53]. In the original design, the pseudorapidity of the RPCs was planned to cover up to $|\eta|<2.1$ [54] but in practice during run 2 they covered the region $|\eta|<1.9$ [53]. In the barrel, there are 4 RPC stations: RB1 and RB2 which are double layered, RB3 and RB4 which are single layered, these go together with the DT stations. In the endcap region there are also 4 RPC stations labeled RE1, RE2, RE3 and RE4. The design of the RPCs consists in units with two parallel plates of bakelite, which is a highly resistive plastic material serving as cathode and anode, these are separated by a gas mixture of 95.2% freon ($C_2H_2F_4$), 4.5% isobutane (C_4H_{10}) and 0.3 % sulphur hexafluoride (SF_6) [52]. One unit is stacked over the other so there are two gas gaps, and between the units a readout strip is installed. A incoming muon would ionize the gas in both chambers, each strip out electron hits other atoms causing an electron avalanche. These electrons are detected by the readout strip. The time for the electrons to drift is well determined, obtaining good spatial and temporal resolution to identify muons. These chambers serve as complementary trigger detectors [55].

4. MEASUREMENTS AND DATA PROCESSING AT THE CMS DETECTOR

4.1 Trigger system

Due to the massive amount events produced in the particle collisions, a trigger system must be implemented to filter the interesting events and keep the data at a reasonable size to be stored and analyzed. The design of the trigger system is different for each detector, in the case of the CMS it has two stages: The Level 1 (L1) trigger and the Higher Level Trigger (HLT) system.

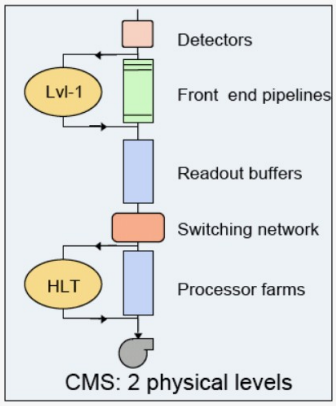

Figure 4.1: Simplified design of the trigger system. From Foudas [56].

First, L1 receives data from the subdetectors, this data is also temporarily stored and processed in the Front end pipelines until the L1 reaches a decision of what data to allow to proceed further, this is the first online data selection. To keep the latency low, the L1 is hardware reliant, using custom made chips to reach a faster selection than software processing would allow. Data then goes to Readout buffers for temporary storage. Switching networks then transfer data to the HLT system, this one does a final software based selection of events relying on a farm of conventional processors [56] [57] but with fast and efficient algorithms in an online selection.

4.2 CMS computing grid

The CMS takes advantage of the Worldwide LHC Computing grid for data processing, reconstruction and analysis. Events in the HLT computer farm are classified in primary data sets. Here, also events with high priority of reconstruction are selected. RAW data from the CMS Online Data Acquisition and Trigger System is transfered to the Tier 0 computing network, located at CERN, is pushed in quasi-real time, here first initial reconstructed (RECO) events are processed. RAW and RECO data are archived, and eventually distributed to the next Tier 1 grid. Also, initial Analysis Object Data (AOD) are produced in tier 0 from the RECO events, the AOD contains important information on the physical objects and a summary of the RECO being more compact than the later. Furthermore, mini-AOD files are generated which are even more compact than AOD, the mini-AOD was introduced in the CMS data flow during Run 2 [59], and a comparison with Run 1 can be seen in figure 4.2:

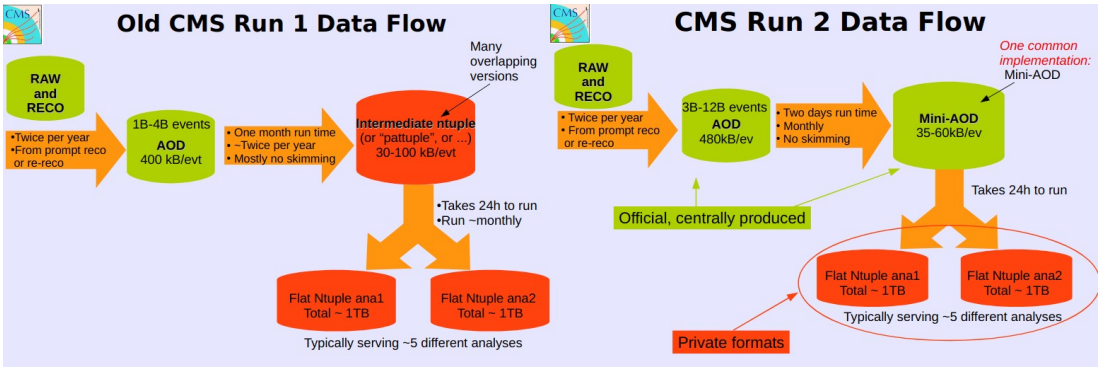

Figure 4.2: Data flow for file storage in CMS. Left: Run 1. Right: Run 2, here the Mini-AOD type is introduced. From G Petrucciani et al [58].

Tier 1 processing centres are computing clusters located in different sites around the world, where further processing is done. Currently there are 13 of these centres, connected to the CERN through an optical-fibre link with a 10 gigabites per second transfer rate [59]. These provide a permanent storage for the produced CMS data. The additional processing power of the Tier 1 is used to mass process all the RAW and RECO data generated and further produce AOD versions. Unlike previous steps, in Tier 1 there is not pressure for low latency processing, here offline reconstruction is done.

Data in Tier 1, can be acceded by smaller, more numerous Tier 2 computer centres, normally run by universities and globally distributed. Here researchers can task analysis like Monte Carlo simulations to compare with provided data. The computing capabilities of the Tier 2 is also available for all the grid [60][61].

4.3 Electron and photon reconstruction

While going through the tracker layer, electrons produce hits, then electrons and also photons deposit most of their energy in the ECAL Reconstruction of signals in the ECAL is done by fitting the signals with templates in order to substract the effect of out-of-time pileup [62]. Before reaching the ECAL, electrons could interact with matter changing their momentum in a bremsstrahlung process while emitting photons, aditionally, these photons could produce an electron-positron pair. This new shower of particles is recombined by an algorithm to recover the momentum and energy of the primary particle. First, the standard procedure for reconstruction will be described in order to introduce some general ideas about this procedure:

The curvature of the electrons when in the tracker is reconstructed using an algorithm based on the Gaussian Sum Filter (GSF), this is used to include losses due to bremsstrahlung. Energy of the electrons and photons is measured in the ECAL, by stopping them, the lost energy then leads to a cascade of secondary electrons and photons, called electromagnetic shower. The sum of energy losses builds up the calorimeter signal. Energy signals are clustered by assuming that a local maximum above a threshold corresponds to a single particle incident in the detector. An signal may be shared by overlapping clusters, but an algorithm is used to determine the fraction of this energy assigned to each cluster. For the aforementioned case of an electron producing a shower of particles before reaching the ECAL, multiple clusters associated to this are combined in a single Super Cluster (SC) to reconstruct the energy of the original electron. These are algorithms are combined with tracking information, using also machine learning techniques for the complete particle reconstruction [62] [63].

Electron tracking starts with choosing the data to do the fitting, these are hits possibly associated with the electron trajectory, the so called “seeding”. A selection could be based on the Tracker or on ECAL signals, this are eventually compared and combined. In any case, the GSF is used on the seeds. The electron track reconstruction is done in a iteration using a Kalman filter. If for a predicted position in a given layer there are several possible hits, then multiple possible trajectories are evaluated. When a given hit is associated to more than one possible trajectory, the one with higher number of hits or lower χ^2 is selected.

For energy reconstruction, one has to consider that a single electron reaching the ECAL can deposit its energy in a number of crystals, given that each deposit is above a threeshold of 1 GeV, these readings are grouped in clusters. But the original electron likely needs to be reconstructed from photons generated by bremsstrahlung radiation which also can produce electron-proton pairs, all depositing energy in other crystal areas. To do so, the produced clusters associated with the original object and its products are to be grouped into a single Super Cluster (SC), in a process called superclustering. The algorithms used to do this combination basically take a cluster which is to be used as a seed, then in an iterative process additional clusters are added if they are likely to be associated with the preceding one, additionally this selection can be polished by taking information from the tracker by finding trajectories compatible with the points where showering was produced. All of this information is also fed to the Particle Flow algorithm to reconstruct the electron. The energy of an electron is obtained from a refined super cluster.

4.3.1 Electron and photon reconstruction for displaced vertices

In this sub-section, the methods and selections for the reconstruction of electrons and photons related to the present work will be briefly summarized. For this case, alternative algorithms to the standard one are used in order to make the search of LLPs more efficient.

Displaced (or secondary) vertices are the spatial origin points of the electrons not directly produced in proton-proton collisions. These are considered when the distance to the primary vertex is measurable in the experiment, like in the case of interest of LLPs, in which case there are optimized algorithms of reconstruction.

The reconstruction of displaced electrons starts by taking reconstructed photons in the CMS, which comes from a ECAL supercluster. These photons are then matched to a track without primary vertex constraint within a $\Delta R<0.1$ cone. Then requirements imposed on the used photons is $E_T>45\,GeV$ for the “leading” and $E_T>28\,GeV$ for the “sub-leading” which is slightly above the requirements of the online reconstruction ($E_T>42\,GeV$ and $E_T>25\,GeV$ respectively). Also for p_T of the tracks the same requirements are imposed, that is, $p_T>45\,GeV$ for the leading and $p_T>28\,GeV$ for the sub-leading one.

4.4 Muon reconstruction

As its name suggest, one of the most important objectives of the Compact Muon Solenoid experiment is precisely the detection of muons. These particles are able to go through several meters of the CMS material without interacting, this is why the specialized Muon detector system is the outermost detector set, electrons also charged elemental particles are stopped earlier in the ECAL facilitating the detection of muons. The track reconstruction is done in two independent

stages depending on where the data comes: the "*tracker muon track*" is provided by the inner tracker and the "*standalone muon track*" is provided by the Muon detector system [52]. Following these stages, two reconstruction methods are used in the standard reconstruction:

- "*Tracker Muon reconstruction*" is done by tacking the tracker tracks with a total momentum magnitude $p > 2.5\,GeV$ and transverse momentum magnitude $p > 0.5\,GeV$, the possible trajectories are prepared using the Kalman filter technique, this data is then extrapolated to the Muon detector system where is compared to the DT or CSC segments. This approach is called "inside-out". A trajectory is accepted if the extrapolated track and the Muon detector system segments differs by less than 3 cm in the *x* coordinate, or if the ratio of this distance to its uncertainty is less than 4 [53].

- "*Global Muon reconstruction*" combines both, standalone muon tracks and tracker muon tracks by fitting signals using a Kalman filter. Trajectories are extrapolated from the innermost chamber in the Muon detector system to the Outer tracker surface [65]. This approach is called "outside-in".

For low momenta, around $p \leq 5\,GeV$, tracker reconstruction is more efficient than global reconstruction since the former needs only a single muon segment, while the later needs muons to penetrate more than one station for optimal performance and this requires higher momentum. On the other hand, the transverse momentum p_t measurement under global reconstruction is better, specially at high momenta such that $p_t > 200\,GeV$. Reconstructed Muon data goes to the particle flow (PF) algorithm.

There is an additional specialized reconstruction algorithm used in this search for LLPs:

- "*Displaced Global Muon (DGM) reconstruction*" as its name implies is optimized for searching displaced muons, that is, muons not produced in the primary vertex. It is implemented in the inner tracker and uses a seed constructed with data from the Muon chambers with constraints for interaction points removed [66]. This algorithm takes the data from the tracker and extrapolates it to the Muon Detector system, increasing momentum resolution for displaced particles over the standard Global reconstruction but for prompt particle its performance decreases. In looking for dimuons, the requeriments imposed is for the particles to be of opposite charge and each track to have a transverse momentum $p_T > 31\,GeV$, slightly above the required online cut of $p_T > 28\,GeV$.

4.4.1 Muon momentum measurement

The momentum measurement of muons in the CMS depends on factors such as the magnetic field, the alignment of the detectors and the interactions with the material. Being charged particles, the trajectory of the muons is affected by the presence of the magnetic field inside the CMS, being the described trajectory dependent on the momentum, the lower the momentum, the more curved is the trajectory. Also the number of layers transversed in the Muon detector system and the produced particle showers in the gas chambers varies with the momentum. An algorithm called *Tune-P* is used to switch between different measurement methods for the transverse momentum, aiming for the most adecuate depending on the detectors readings. This is a complex problem but a calibration has been done in the CMS thanks to the phenomena of cosmic ray muons [67].

4.5 Vertex reconstruction

The objective of the vertex reconstruction techniques is to find the generating point in space of the particles. The base is of this type of reconstruction is the fitting of particles trajectories using a Kalmar filter. The algorithm has to take a set of trajectories and choice those associated with the particle of interest, reducing the presence of data associated with other particles trajectories. The used algorithm depends on the type of vertex.

4.5.1 Primary vertex reconstruction

This aims for the vertex associated to the original proton-proton collision. It starts by taking the reconstructed LHC beam spot, this is the center of the luminosity region of the opposite accelerated beams in the place of collision. This is not necessarily where the proton-proton collision occur but it must be at least very close, considering this, the algorithm imposes a limit to the impact parameter of the track. The standard CMS algorithm requires impact parameter less than 5 cm, at least 2 hits in the pixel layers, at least 5 hits in the pixel+strip layers [68]. This reconstruction will be later used as basis for secondary vertex reconstruction too, so for searching LLPs a stricter criteria is used to obtain the primary vertex: impact parameter less than 2 cm, no more than 24 cm apart in the direction of the beam and be associated with at least 4 tracks [64]. The selected tracks are then clustered according to their z coordinates, the beams are bunches of particles and when opposing beams encounter each other, multiple proton-proton collisions can happen, so the clustering is for discerning these collisions. Next, the possible vertex associated with at least 2 tracks are fitted using an "*adaptative vertex fitter*" algorithm, this gives to each track in the vertex a value from 0 to 1, being 1 the highest likeness for the track to correspond to the vertex, the total number of the tracks for this vertex is also calculated using that assigned value as a weight in the calculation.

4.5.2 Secondary vertex reconstruction

A secondary vertex reconstruction aims for determining the spatial origin of particles which are not produced directly in a proton-proton collision but in a later process, given that its separation from the primary vertex is measurable in the experiment. For their reconstruction, the "Trimmed Kalman Vertex Fitter" (TKFT) is used, then the vertex candidates are evaluated based on their distance to a primary vertex and an upper cut on the invariant mass [69]. In the search for LLPs, vertices of leptons are reconstructed from tracker data within a pseudorapidity region $|\eta|<2$, since the efficiency falls for large $|\eta|$ values [64].

4.6 Dilepton reconstruction and selection in search for Long Lived Particles

For a LLP decay in this analysis, dileptons are expected. The leptons are paired by selecting tracks of the same flavor and opposite charge, then performing a fit, using an Adaptative Vertex Fitter algorithm, to a common displaced vertex. The requirements imposed in this reconstruction are a pseudorapidity region $|\eta|<2.0$, a $\chi^2/(number\ of\ degrees\ of\ freedom)$ ratio less than 10 for the vertex, a low mass rejection of $m_{ll}<15 GeV$ and for the leptons to be of opposite charges. Also it is required for the leading and sub-leading dimuon to have $p_T>31 GeV$, and for the leading (sub-leading) dielectron to have $p_T>45 GeV\,(28 GeV)$. The *collinearity* variable $\Delta\Phi$ must also have an absolute value less than $\pi/2\,rad$. Since the Z boson production is the most important background source here, there is a reconstruction in the so called "Off-Z region" in which the region where the Z boson mass resonance is expected (91 GeV) is avoided by imposing a $|91-m_{ll}|>10 GeV$ cut-off, in the reconstruction shown in the incoming chapter 5 this last

requirement will not be used but results for the Off-Z region are included in the annexes. These requirements and some others are summarized in the table 4.1.

Dimuon selection	Dielectron selection
• Leading p_T > 31 GeV	• ECAL Leading p_T > 45 GeV
• Subleading p_T > 31 GeV	• ECAL Subleading p_T > 28 GeV
• |η| < 2.0	• Leading E_T > 45 GeV
• Vertex χ^2/ndof < 10	• Subleading E_T > 28 GeV
• Angular distance ΔR < 0.2	• |η| < 2.0
• cos(α) > -0.8	• |η| not in [1.4442, 1566]
• Relative PF Isolation < 0.2	• Vertex χ^2/ndof < 10
• Low-mass rejection m_{ll} < 15 GeV	• Relative Tracker Isolation < 0.1
• OS-sign charge	• Low-mass rejection m_{ll} < 15 GeV
• Forward region: |ΔΦ| < π/2	• OS-sign charge
• Off-Z region: |91 − m_{ll}| > 10 GeV	• Forward region: |ΔΦ| < π/2
	• Off-Z region: |91 − m_{ll}| > 10 GeV

Table 4.1: Dimuon and dielectron reconstruction selection.

For tracks, the analysis in which this work is based uses as initial approach an impact parameter significance d_{xy}/σ greater than 6 for both electrons and muons.

5. ANALYSIS

The analyzed data is from the Run 2 of the LHC, obtained in 2016 by the CMS experiment using proton-proton collisions at a centre-of-mass energy of 13 TeV (see Table 3.1). A model is used in which a non-Standard Model Higgs (BSM H) produced two spinless X bosons and these then produce SM leptons, particularly electrons and muons as in Figure 2.2. For this model, generated Monte Carlo samples are generated with PYTHIA v8. In this analysis some possibilities for the masses of the BSM H and X bosons are considered.

Here, X bosons are explored as LLPs so the lepton production would be in a secondary, displaced vertex with respect to the primary vertex where the bosons are generated. That is, the flight distance of the X bosons is of special interest.

In this analysis, different signals will be used, which correspond to $H \rightarrow XX \rightarrow l^- l^+ l^- l^+$ processes as shown in figure 2.3. Each signal corresponds to given initial parameters of Higgs boson mass, X boson mass and X boson mean lifetime. First, in section 5.1 Monte Carlo simulations will be presented for different variables at generation level, then in section 5.2 plots for reconstruction of different sets of signals are analyzed, as well as a figure of merit for them. Finally, in section 5.3 the flight distance and impact parameter at generation level are briefly compared.

5.1. Modeled parameters

Monte Carlo samples were generated for different signals and different measurable variables were explored, each signal assumes different H and X masses and mean lifetime for X. These simulations are at generation level, that is, here the reconstruction efficiencies are not taken into consideration. The objective of this section is to explore the kinematics and displacement for the different signals presented in table 5.1:

H mass (GeV)	X mass (GeV)	X mean lifetime (mm)
1000	150	100
1000	350	350
400	150	400
400	50	40

Table 5.1: Chosen parameters for different signals used

From here, signals will be referenced in the (H mass)_(X mass)_(H mean lifetime) format.

Let us start by looking at the plots related to the linear momentum. In figure 5.1 histograms are shown for the magnitude of the projection of the momentum in the xy plane, that is, the “transverse momentum” magnitude.

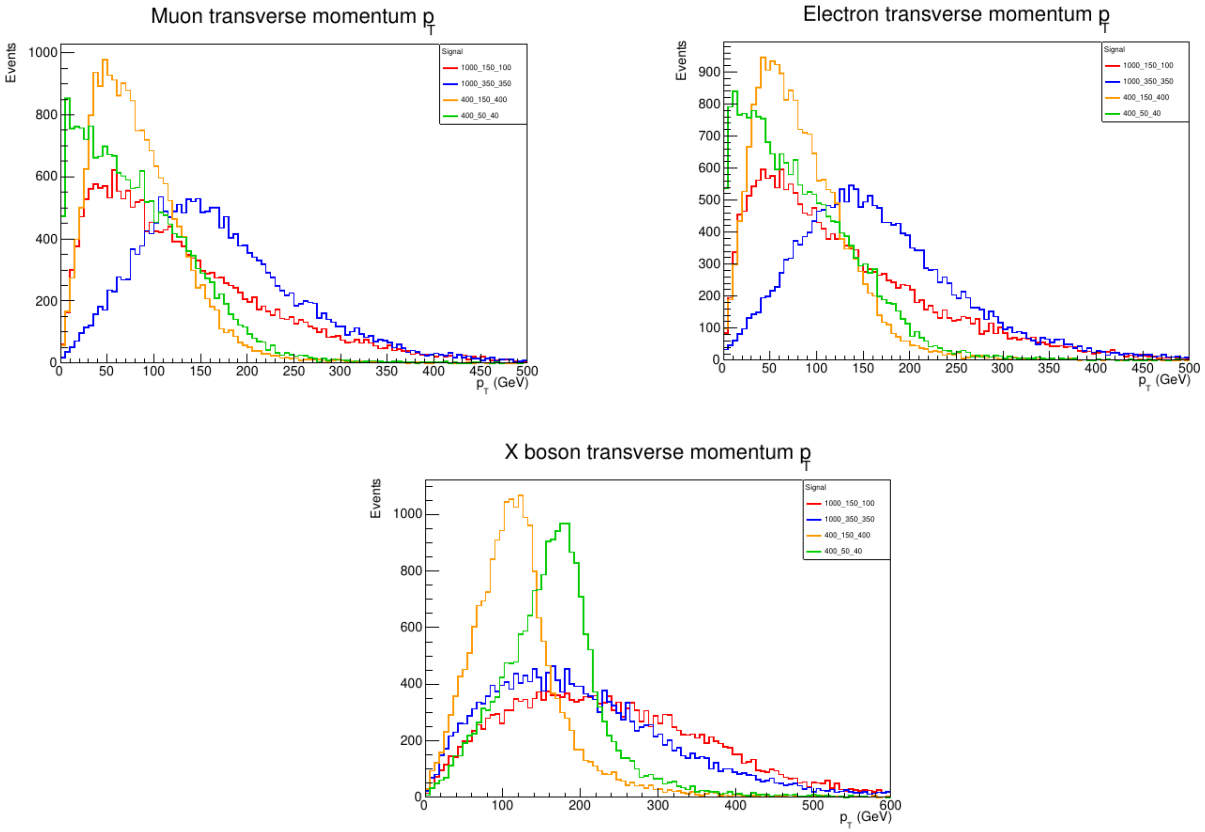

Figure 5.1: Magnitude of transverse momentum. Upper left: Muons, Upper right: Electrons, Bottom: X bosons.

From these histograms, it is already possible to see that the kinematics for each signal is distinct. The 400_50_40 signal tends to produce to produce the leptons with lesser momenta than others but in the plot for X bosons it shows a momentum with a maximum almost aligned with the maximum of the signals with Higgs mass of 1000 GeV. Also, in this sample of 4 signals, those with more massive X bosons tend to produce leptons with more momenta.

For leptons there is some displacement for the maximum for different signals, the earlier maximum is at $p_T \approx 10\,GeV$ for the 400_50_40 signal and the later maximum is at $p_T \approx 150\,GeV$ for the 1000_350_350 signal.

In the case of the X boson, the maximum for the different signals is not as separated in comparison, the left-most at $p_T \approx 100\,GeV$ corresponds to the 400_150_400 signal the other three signals have their maxima almost aligned reaching up to $p_T \approx 200\,GeV$, also the signals with higher Higgs boson mass in this set are more flat in their p_T .

As expected, energy also shows a different curve for each signal as seen in figure 5.2, this time the histogram for the Higgs boson is included.

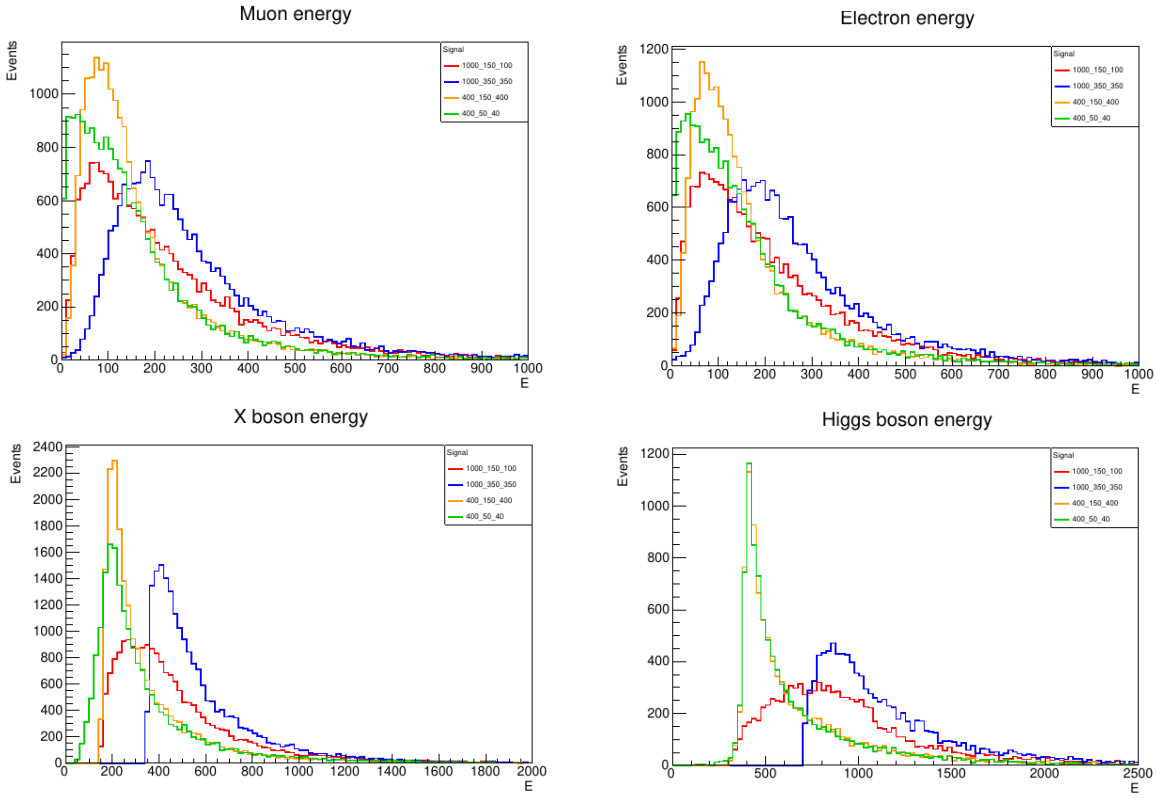

Figure 5.2: Energy. Upper left: muon, Upper right: electron, Bottom left: X boson, Bottom right: Higgs boson.

In figures 5.1 and 5.2 it can be seen how similar are the resulting electrons and muons in their kinematics. In these signals set, the Higgs and X boson energy tends to be higher for signals in which particles have more mass, although the difference between 400_50_40 and 400_150_400 signals is small, so there is no linearity in this correlation. In the case of leptons, we can see how each signal peaks at around half the X boson mass, this is to be expected in a two body decay where the produced particles have the same mass [70].

Let α be the angle between leptons with the same origin (a dilepton), as in figure 5.3:

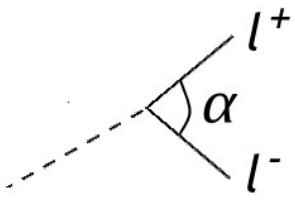

Figure 5.3: Angle between leptons.

To explore this for different signals, one has to consider that there are three possible combinations for the produced leptons in our process of interest, because here each X boson could produce either a electron-positron pair or a muon-antimuon pair, this is shown in figure 5.4.

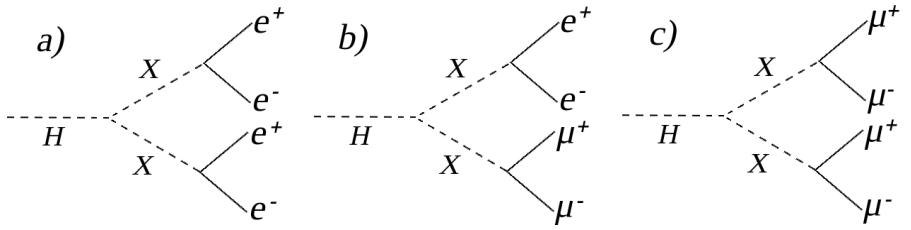

Figure 5.4: Different possibilities for the leptons produced by the X bosons.

For a final state with $e^-e^+\mu^-\mu^+$ as in figure 5.4.b, the angle α of the desired dilepton is calculated from the linear momentum vectors of both same-flavor leptons.

But the other two cases introduce a problem since for a given lepton it is necessary to determine which other lepton comes from the same X boson, here an iterative comparison was used to deal with these combinations. The approach used if the process were like figure 5.4.a or like figure 5.4.c was to take all possible pairs of leptons and obtain the sum of their momenta, then this was compared to the momentum of both possible parent X bosons and the angle obtained. The lowest angle was associated to the process $X \rightarrow l^- l^+$, and for this lepton pair the angle was obtained by using the momentum information of each particle.

The results for the angle α are shown in figure 5.5:

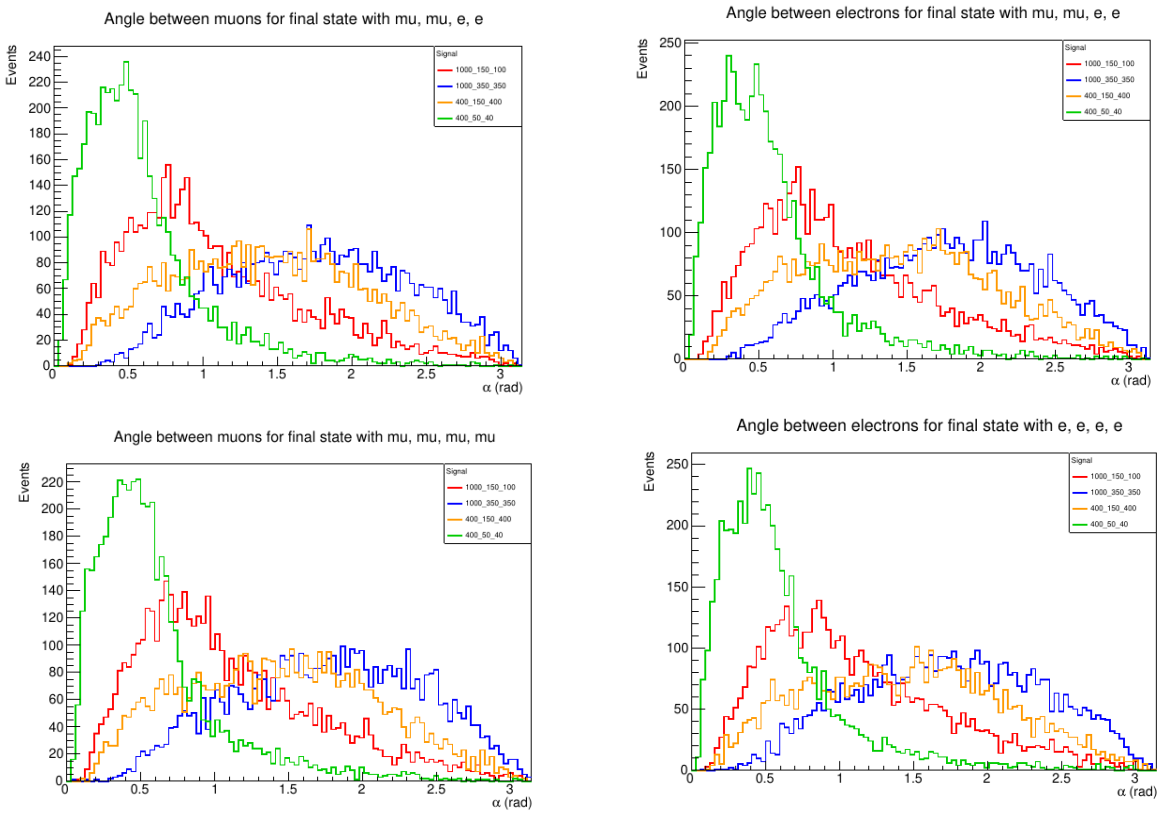

Figure 5.5: Angle α for dileptons.

As can be seen, the dileptonic angle α for a given signal has a shape which is similar for the different cases considered, that is, the α angle does not depend on the final products. This was expected but the distinction was made in order to be able to consider separately reconstruction for $XX \rightarrow e^- e^+ e^- e^+$, $XX \rightarrow e^- e^+ \mu^- \mu^+$ and $XX \rightarrow \mu^- \mu^+ \mu^- \mu^+$, this could be relevant for acceptance studies. Regarding the signals, here the 400_50_40 one is much less evenly distributed than the other signals, with a tendency to peak around 0.4 rad.

Pseudorapity has been simulated in the case of the X boson as seen in figure 5.6. The distribution shows a symmetry around zero as no bias is expected. The 1000_350_350 and 400_150_400 signals have the feature of being almost flat in the $|\eta|<1$ region.

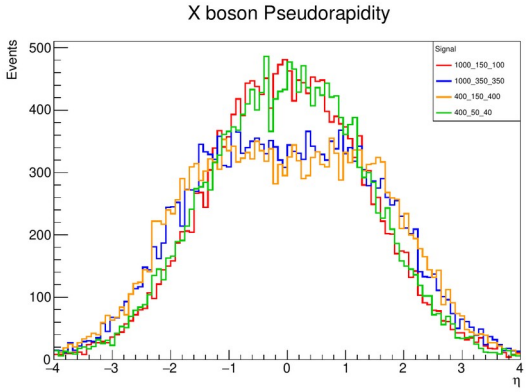

Figure 5.6: Pseudorapidity of X boson.

As the X boson would not be directly observed, it is important to look at the pseudorapidity of the electrons and muons it could produce, as these are detected by the tracker, ECAL and the Muon Detector system respectively. Pseudorapidity for these particles is shown in figure 5.7.

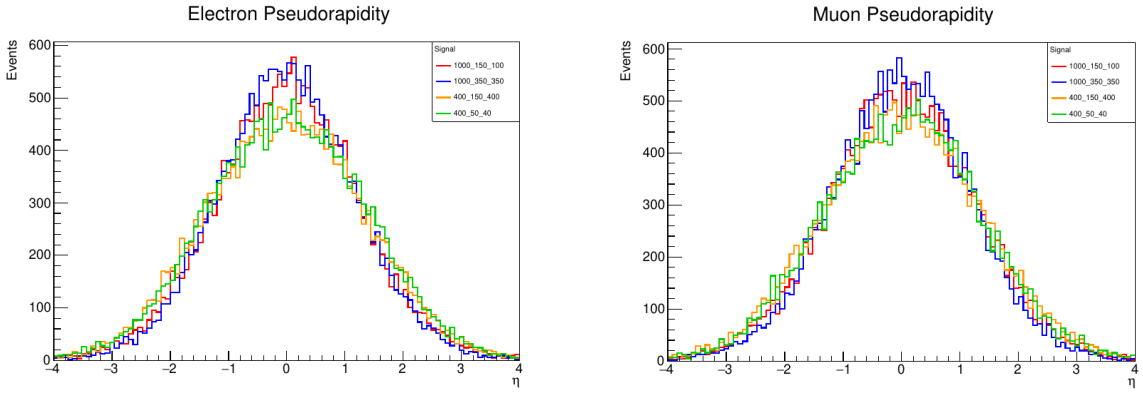

Figure 5.7: Pseudorapidity. Left: electrons. Right: muons.

In both cases η has a symmetric distribution with maximum around zero. Looking at the distribution in these simulation, one has to remember that the ECAL covers the region $|\eta|<3$, also the Muon detector system covers $|\eta|<2.4$, while at reconstruction level there is a more strict cut for $|\eta|<2.0$ so most of these leptons will be detectable.

The flight distance for the X boson is simulated for two different cases: for electron production and for muon production. The results are shown in Figure 5.8:

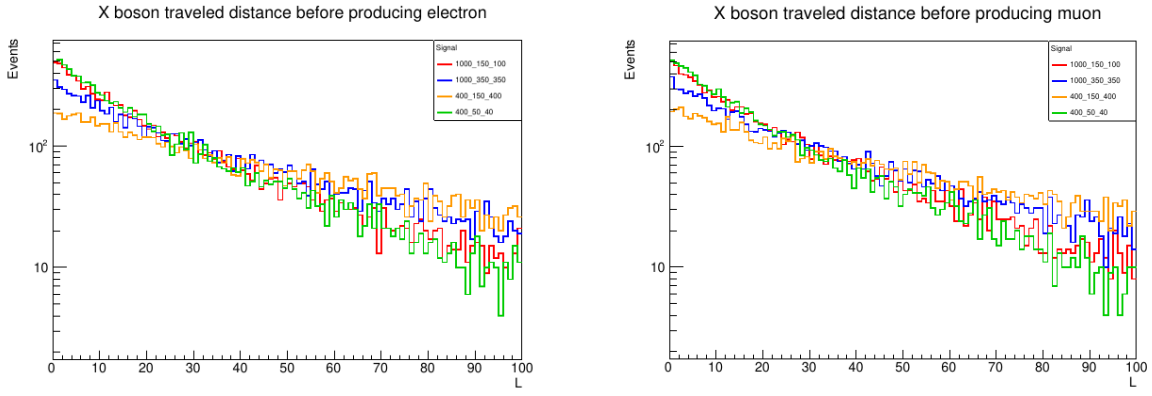

Figure 5.8: flight distance for the X boson when producing: a) electron, b) muon.

Flight distance shows a exponential-like decreasing distribution, what is seen here is a LLP that would be able to produce distinctively separated dileptons in a secondary vertex. As expected, for larger values of mean lifetime, the flight distance tends to go further.

Until this point, at generation level, simulated variables for electrons and muons show a similar behavior. This suggests us that it would be possible to conduct a search of this type based in only one kind of lepton if that where necessary, as physics does not significantly change. However, there are appreciable differences between electrons and muons at reconstruction level, as we will see in section 5.2.

For different signals, the gamma factor of the X boson is also generated as shown in Figure 5.9.

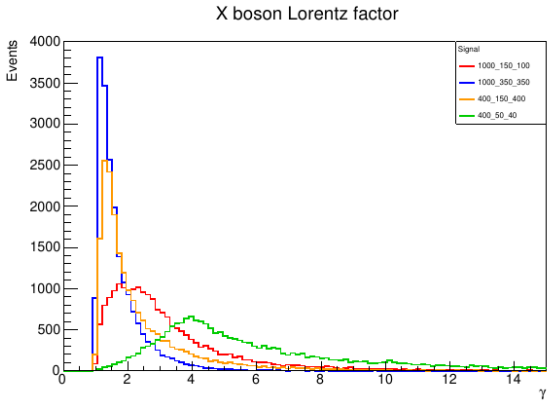

Figure 5.9: Lorentz factor of X boson.

For these 4 signals we see that the lower is the ratio of X boson mass to the parent Higgs boson mass, the faster is the speed of the X boson. In this sample set, the 400_50_40 signal clearly tends to be the most relativistic, followed by the 1000_150_100 signal. When comparing this with figure 5.5 we can see how the more boosted the signal, the lower tends to be the α angle, as expected.

5.2. Reconstruction

In this section, the reconstruction for a given set of signals will be explored and compared. Until now we have seen how our samples have diverse displacement and kinematics, and the efficiency of reconstructions for displaced vertices have an important dependence on these aspects [71], that is why here we will try to look to optimize the displacement criteria for these diverse signals. The selection used in this process is the one introduced in section 4.6. When analyzing the signal is important to take into consideration other processes that would lead to the same products as the process of interest, this additional signal is the called "*background*". For our case, background would mainly be due to: QCD, Drell-Yan, W+jets, Dibosons (WW, WZ, ZZ) and TT jets.

The analysis in which this work is based uses the data to estimate the background by means of *collinearity,* which refers to the angle $\Delta\Phi$ between the transverse momentum of a dilepton and the vector joining the primary vertex with the secondary vertex. If a dilepton is not generated by the X boson, the angle can take any value thus having a uniform distribution in the range $-\pi<\Delta\Phi<\pi$. The signal region is reconstructed with a cut of $|\Delta\Phi|<\pi/2$ as said in section 4.6, and the background contribution is estimated from data using a background control region defined by inverting this cut with $|\Delta\Phi|>\pi/2$.

The main objective in this part is to explore the transverse flight distance L_{xy} , and transverse impact parameter d_{xy} , which is defined as the shortest distance between the primary vertex and the reconstructed track belonging to the dilepton [72]. Also a figure of merit will be used as a way to optimize the cut on the displacement variable for each signal.

Another variable that will be analyzed is the quantity I_{xy} , related to the transverse flight distance and defined as:

$$I_{xy}=\frac{|L_{xy}|}{\sigma_L} \tag{5.1}$$

where σ_L is the error of L_{xy} .

Here also the quantity $d_{xy}/\sigma(d_{xy})$ will be used, where $\sigma(d_{xy})$ is the error of d_{xy} . In a dilepton, each lepton have its own $d_{xy}/\sigma(d_{xy})$, in this reconstruction the minimum of the two possible values is used. Furthermore, if there is more than one dilepton candidate (each one with its own minimum $d_{xy}/\sigma(d_{xy})$ already selected), then the dilepton with higher $d_{xy}/\sigma(d_{xy})$ is chosen. The set of signals to be used in this section is summarized in table 5.2.

H mass (GeV)	X mass (GeV)	H mean lifetime (mm)	Cross section (fb)
1000	350	350	0.3825
1000	350	35	0.3825
1000	150	100	0.7739
1000	150	10	0.7739
400	150	400	677.3
400	50	400	632.1
400	50	40	632.1
400	50	4	632.1

Table 5.2: Set of all reconstructed signals.

Since the signals with 400 GeV Higgs mass will be much higher than for those with 1000 GeV Higgs mass (due to the much larger cross section. See Table 5.2), these will be separated in two sets and examined separately, that is, a set with low Higgs masses and a set with high Higgs masses.

Also, the electron and muon channel will be separated, as it will be seen, this time around we have a difference in lepton flavor. This is because in the experiment the muons are not as affected by bremsstrahlung radiation.

For this reconstruction the cut $|91-m_{ll}|>10GeV$ will not be used, but an Off-Z reconstruction (see section 4.6) could be useful for eliminating Drell-Yan background, in figure 5.10 we can see a the Off-Z $d_{xy}/\sigma(d_{xy})$ reconstruction in the electron channel for the low set, which could be compared to the reconstruction without the $|91-m_{ll}|>10GeV$ cut in figure 5.11 (bottom right). Here an important reduction in the background can be seen. However we decided to continue with the optimization study without the application of the Off-Z cut in order to have more events available to describe the background shape and avoid fluctuations. In the annexes more plots for the Off-Z reconstruction are included.

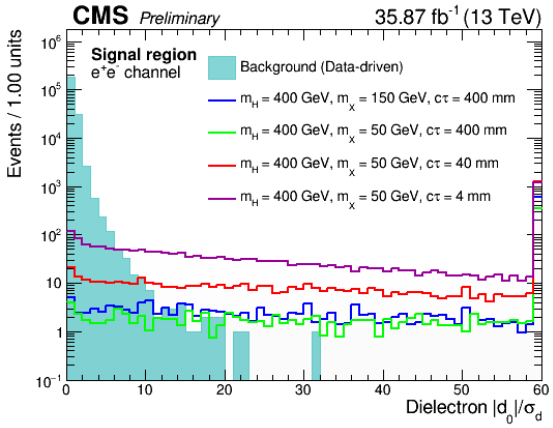

Figure 5.10: Off-Z region reconstruction in electron channel for the case of Higgs boson mass = 400 GeV for the $d_{xy}/\sigma(d_{xy})$ variable.

For the electron channel, in the low set we have for L_{xy} , I_{xy} , d_{xy} and $d_{xy}/\sigma(d_{xy})$ the results shown in figure 5.10.

In the case of L_{xy} , three of the signals surpass the background beyond 10 cm, only the one with shortest mean time, the 400_50_4 signal, does not separate as clearly from the background. In this sample set, the 400_50_40 is the highest in a short interval until $L_{xy}\approx 35\,cm$ where it is overtaken by the 400_50_400 signal. To have a better grasp of what an optimal cut would be, a figure of merit based on the signal and background after selection will be introduced later.

For the I_{xy} variable, we are looking at something different. This time the flight distance goes divided by the error, the 400_50_4 signal shows to have the larger value of I_{xy} in all the considered range, and above the background after $I_{xy}\approx 30$, unlike the case of L_{xy} where this particular signal does not separate as clearly of the background.

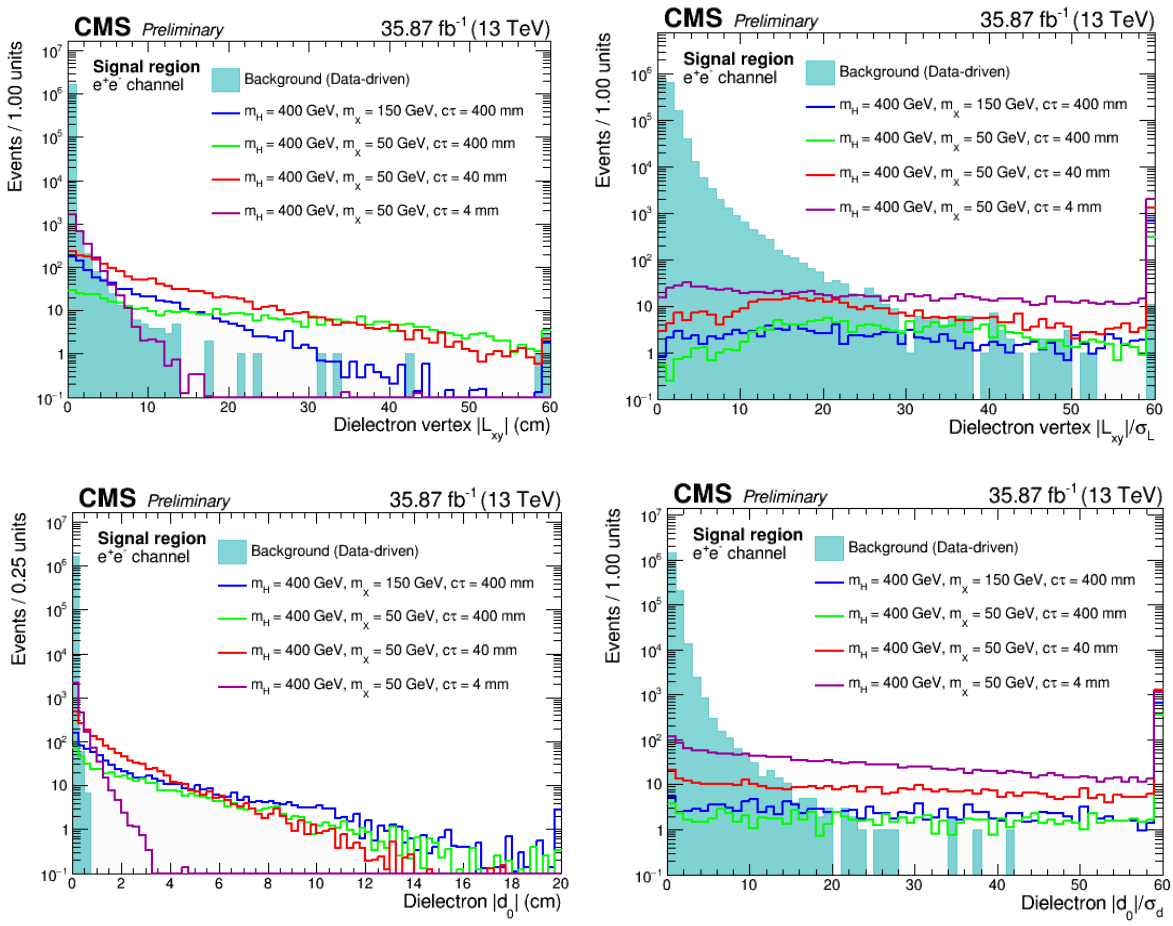

Figure 5.11: Reconstruction in electron channel for the case of Higgs boson mass = 400 GeV. Upper left: L_{xy} , upper right: I_{xy} , lower left: d_{xy} , lower right: $d_{xy}/\sigma(d_{xy})$.

Looking at d_{xy} , it tends to go higher for signals with a larger mean life time. This variable that shows a negative exponential-like behavior for the number of events, with the 400_50_4 signal falling more rapidly than the others, as to be expected since it has the lowest lifetime.

The $d_{xy}/\sigma(d_{xy})$ variable, like the I_{xy} , changes the ordering if the signals, this time the 400_50_4 stays above the rest and goes above the background after $d_{xy}/\sigma(d_{xy}) \approx 10$. This time the 400_50_40 signal also surpasses clearly the background after $d_{xy}/\sigma(d_{xy}) \approx 15$.

Next, in figure 5.12 we see the information but for muons, the general shape of the histograms resemble those for the electron. The general interpretation given for electron generation still applies, with differences in the number of events and values for which the background is surpassed. For L_{xy} and d_{xy} in the case of muons the curves go higher than for electrons in the considered region. This is in contrast with the observation at generation level in section 5.1 that electrons and muons are produced in a very similar way, for example figure 5.8. This is due to differences in the efficiency of reconstruction between electrons and muons.

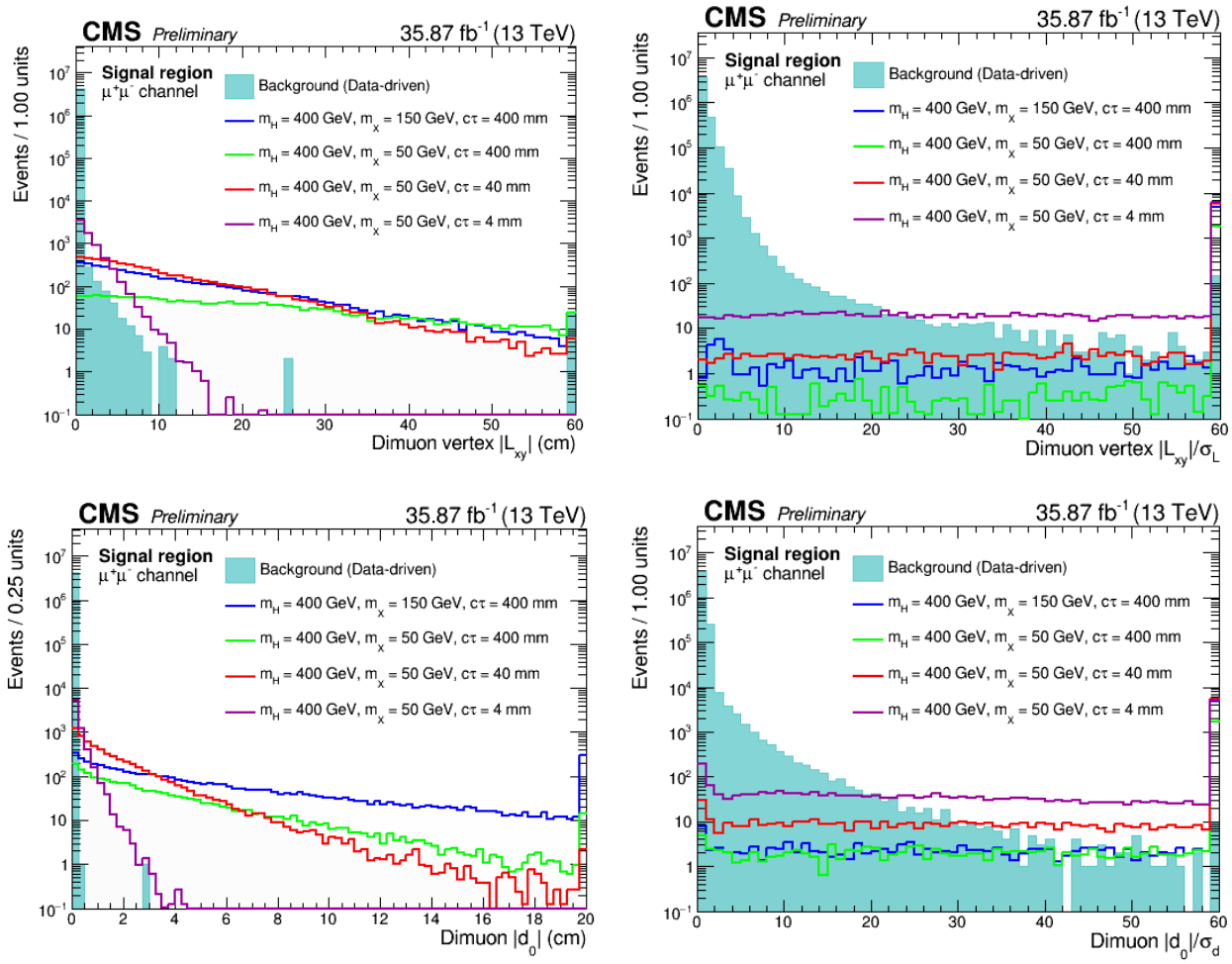

Figure 5.12: Reconstruction in muon channel for the case of Higgs boson mass = 400 GeV. Upper left: L_{xy} , upper right: I_{xy} , lower left: d_{xy} , lower right: $d_{xy}/\sigma(d_{xy})$.

At this point then, it is important to introduce a figure of merit called "*signal significance*" [73], defined as:

$$FoM = \frac{S}{\sqrt{S+B}} \tag{5.2}$$

Where *S* is the expected signal above a given value for the considered variable and *B* is the expected background above the same value. This figure of merit is commonly used in particle physics to express cleanliness of a signal. For these plots *S* and *B* are obtained by taking the area of the respective signal and background curves to the right of each bin in the histogram of the variable of interest.

The signal significance has been calculated for each variable, the results for the electron case from signals with m_H = 400 GeV are summarized in the figure 5.13.

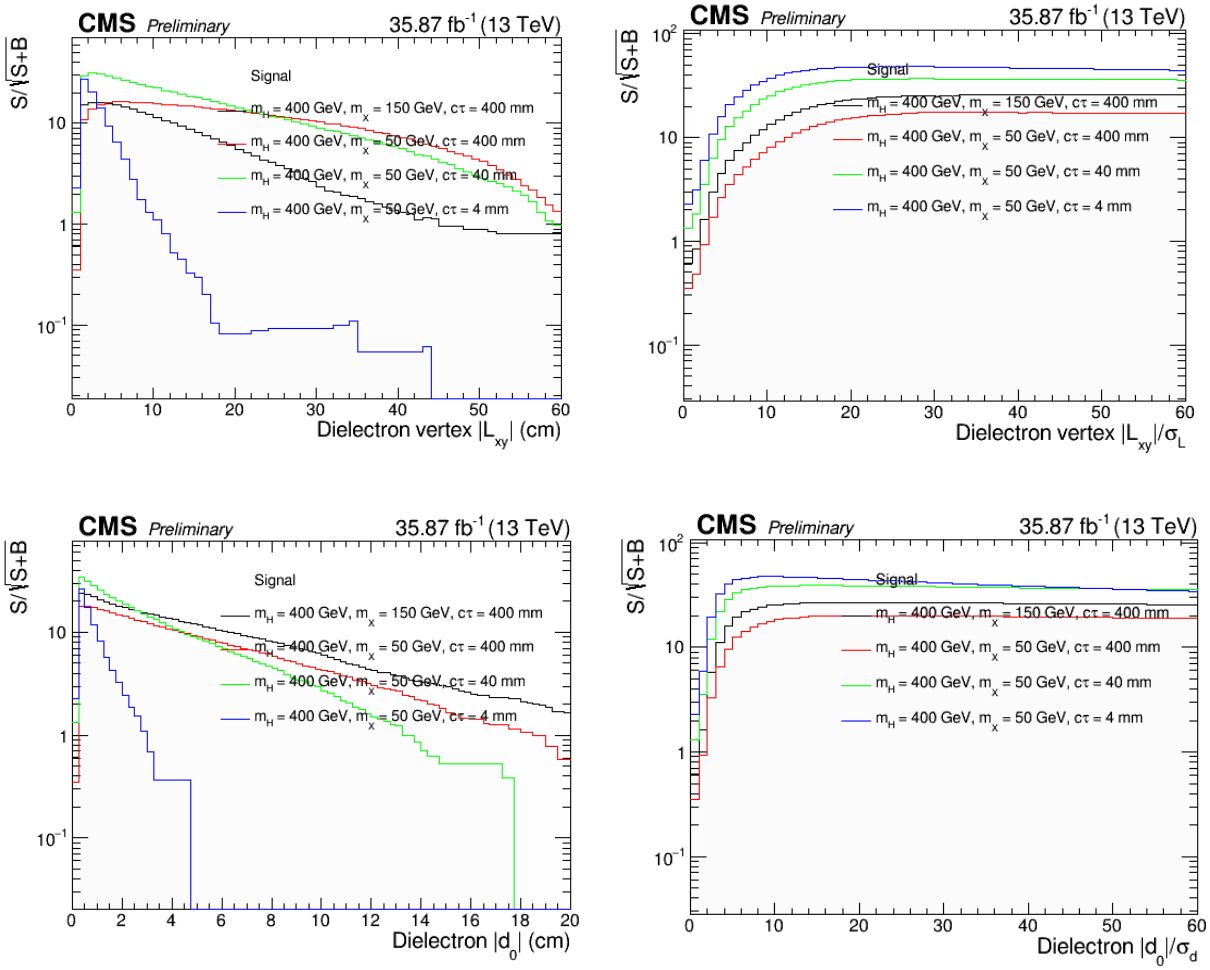

Figure 5.13: Signal significance in electron channel for the case of Higgs boson mass = 400 GeV. Upper left: L_{xy} , upper right: I_{xy} , lower left: d_{xy} , lower right: $d_{xy}/\sigma(d_{xy})$.

For L_{xy} the signal significance is at its highest very early just at $L_{xy} \approx 5-7\,cm$ for the 400_50_400 signal, $L_{xy} \approx 1-3\,cm$ for most of the others before starting to fall. The 400_50_4 signal goes down more abruptly than the others. The other signals keep a higher value, for example at $L_{xy} \approx 15\,cm$ all three of them are still above double digit figures of signal significance.

The I_{xy} variable, as seen in the figure above, presents have a stable significance above $I_{xy} \approx 20$ for all signals, with a $FoM > 10$ until the end of the considered range at $I_{xy} = 60$. Under the signal significance criteria, I_{xy} is a variable with a good discrimination that could be considered in LLPs searches.

In the case of impact parameter d_{xy} the signal significance falls very quickly for the 400_50_4 signal, in this case a very narrow cut of $0 < d_{xy} < 1-2\,cm$ would have to be used for a clear signal. The other signals keep falling from a initial high value when $d_{xy} \approx 1-2\,cm$ and go below $FoM = 10$ at $d_{xy} \approx 10\,cm$. Also, the maxima of the signals for this figure of merit is on the same order of magnitude than in the case of L_{xy} and both variables show a similar behavior here.

In the remaining plot of figure 5.13, we see how the figure of merit of $d_{xy}/\sigma(d_{xy})$ is stable beyond $d_{xy}/\sigma(d_{xy}) \approx 10$ and what was said for I_{xy} also applies here; the signal significance for $d_{xy}/\sigma(d_{xy})$ is considerably good for the given set of signals and the both behave similarly and have maxima in the same order of magnitude for this set of signals. Also notice that the stable maxima (for the considered range) in the case of these $d_{xy}/\sigma(d_{xy})$ and I_{xy} is of the same order of magnitude than the maxima for the L_{xy} and d_{xy} cases.

The same figure of merit criteria is applied to the muon channel and the results are shown in figure 5.14:

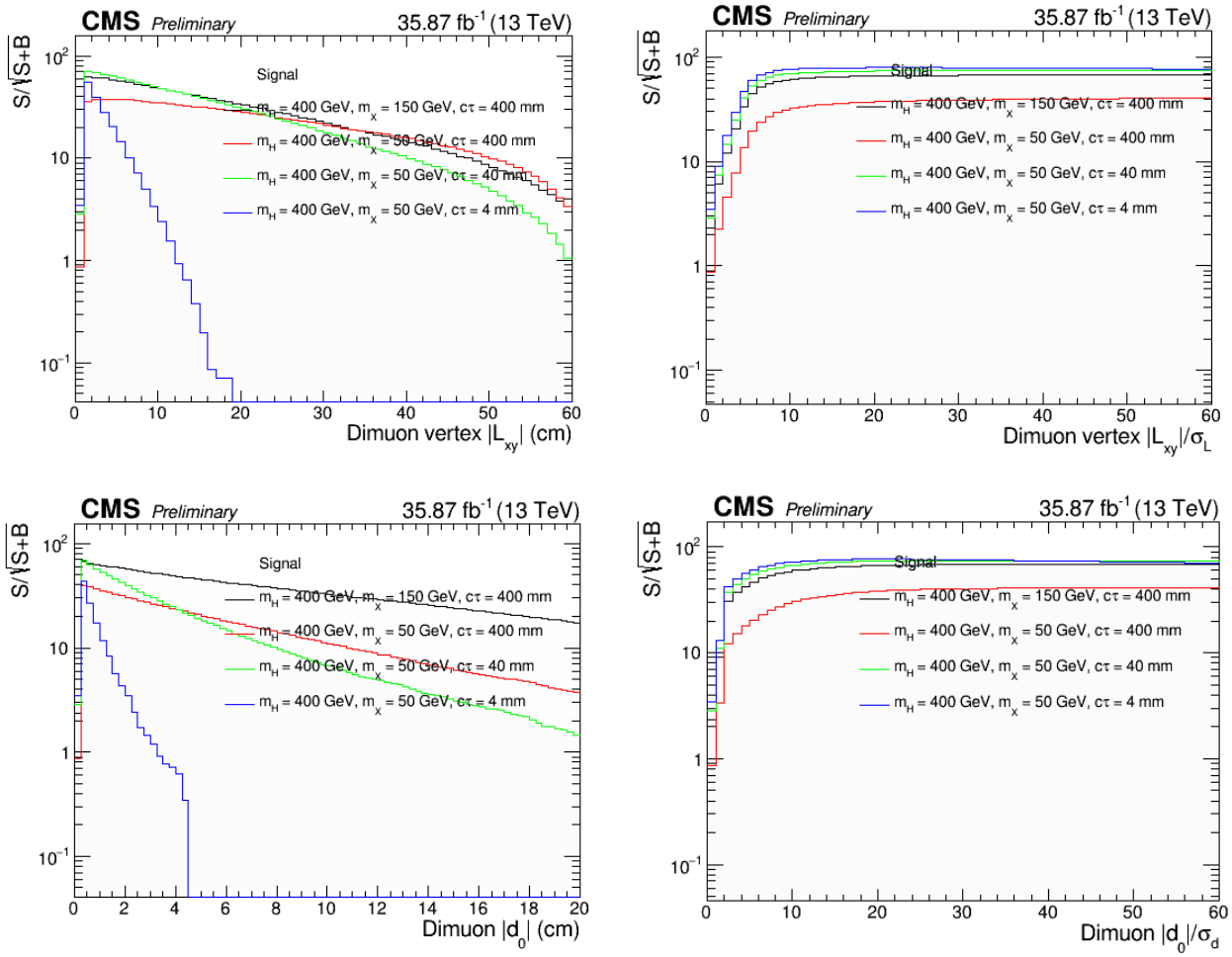

Figure 5:14: Signal significance in muon channel for the case of Higgs boson mass = 400 GeV. Upper left: L_{xy}, upper right: I_{xy}, lower left: d_{xy}, lower right: $d_{xy}/\sigma(d_{xy})$.

The shapes of the curves are similar to the electron channel and the general description of the signal significance for the considered variables remain the same, as well as the observation that the figure of merit for I_{xy} and $d_{xy}/\sigma(d_{xy})$ is high and stable in a wide range. What is different and noteworthy for this channel is the higher value in general for our figure of merit in comparison to the electron channel. This holds for all the considered variables and signals, reinforcing what was said before that reconstruction in the muon channel is more efficient for the analysis done here.

Now the remaining signals, those coming with a Higgs boson mass of 1000 GeV, which is our high set, will be reviewed in the same way. Starting with the electron channel, for the reconstruction of L_{xy} , I_{xy} , d_{xy} and $d_{xy}/\sigma(d_{xy})$, the results are summarized in the plots shown in figure 5.15.

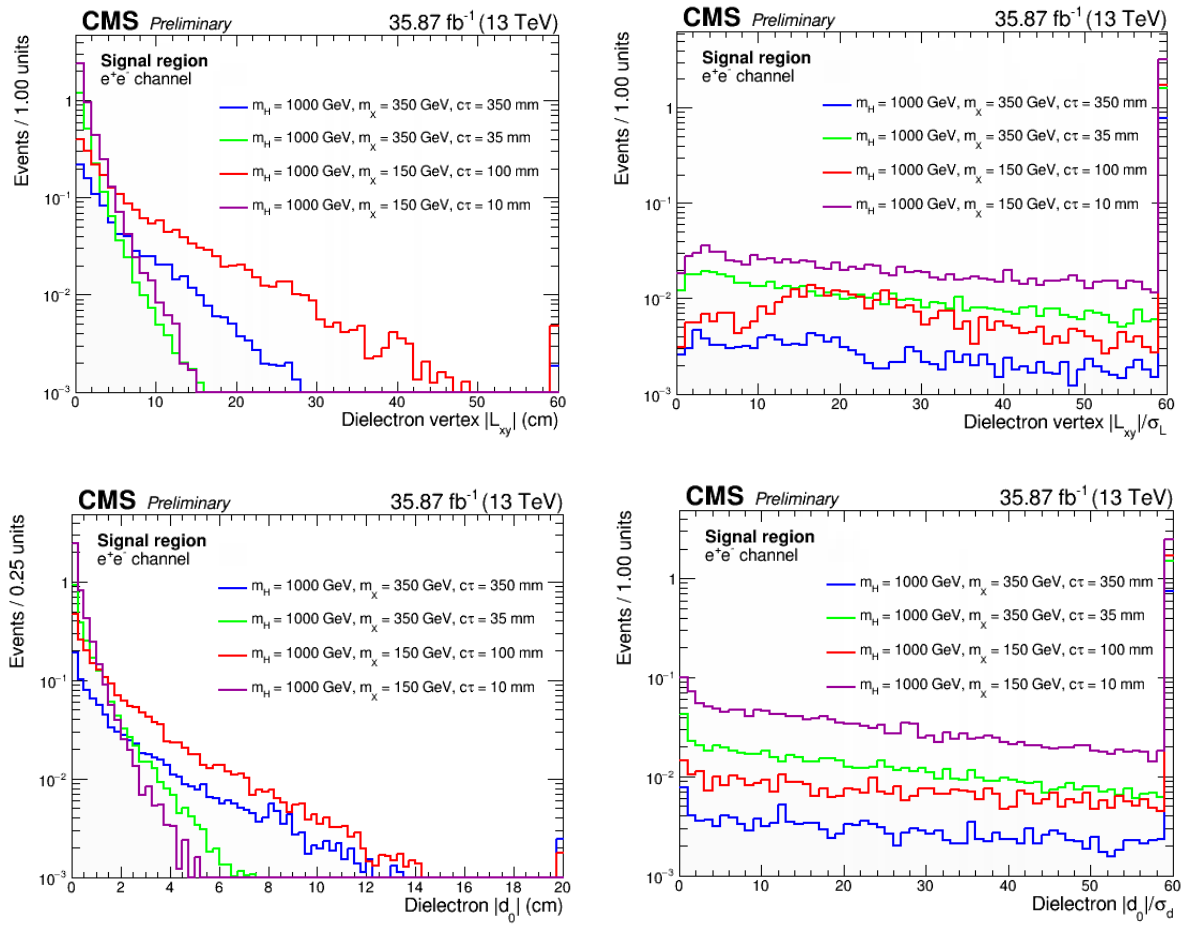

Figure 5.15: Reconstruction in electron channel for the case of Higgs boson mass = 1000 GeV. Upper left: L_{xy} , upper right: I_{xy} , lower left: d_{xy} , lower right: $d_{xy}/\sigma(d_{xy})$.

The first thing that becomes manifested in these plots is that the number of events is much lower for all the variables and signals than in the lower set. Also, the background in these plots is not included because is several orders of magnitude higher than the signals, unlike the case of the electron channel for the lower set in figure 5.11 where signal and background where comparable.

For L_{xy} we see above a negative exponential-like behavior. The 1000_350_350 signal is the one that goes further followed by the 1000_150_100 one, as expected, because those are the signals with the highest mean life-time in the set. The other two signals however, do not follow these expectations as the 1000_350_35 is below the 1000_150_10 in most of the range, but the number of events is very low in any case and this could be due to statistical fluctuations.

The I_{xy} , d_{xy} and $d_{xy}/\sigma(d_{xy})$ variables have similar shapes to those for the lower set as seen in figure 5.11, but as said before, with much less events, the difference tends to be of 2 or 3 orders of magnitude.

Similar results to those above are obtained for the muon channel as seen in figure 5.16, again with a low number of events for all signals.

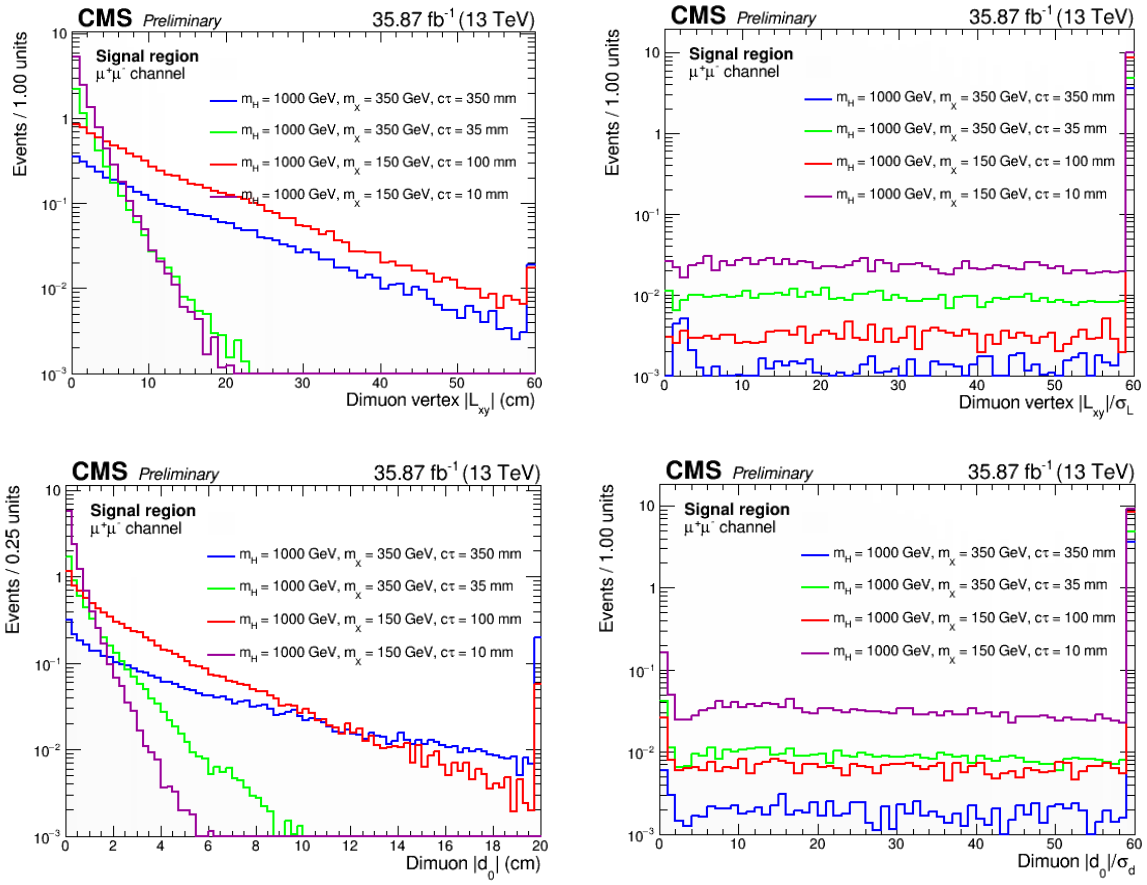

Figure 5.16: Reconstruction in muon channel for the case of Higgs boson mass = 1000 GeV. Upper left: L_{xy} , upper right: I_{xy} , lower left: d_{xy} , lower right: $d_{xy}/\sigma(d_{xy})$.

In comparing figures 5.15 and 5.16, the differences are mostly in the number of events and not the shape of the signals, particularly for the L_{xy} and d_{xy} variables we can see a tendency to have more events, up to around 1 order of magnitude above in the muon channel compared to the electron channel. This was also previously found to happen in the low set of signals.

For the I_{xy} and $d_{xy}/\sigma(d_{xy})$ variables in figure 5.16 we can see, similarly to the electron channel in figure 5.15, stability in the signals for the considered region.

The same figure of merit defined in (5.2) is applied to this set of 4 signals, and results for the electron channel are shown in figure 5.17.

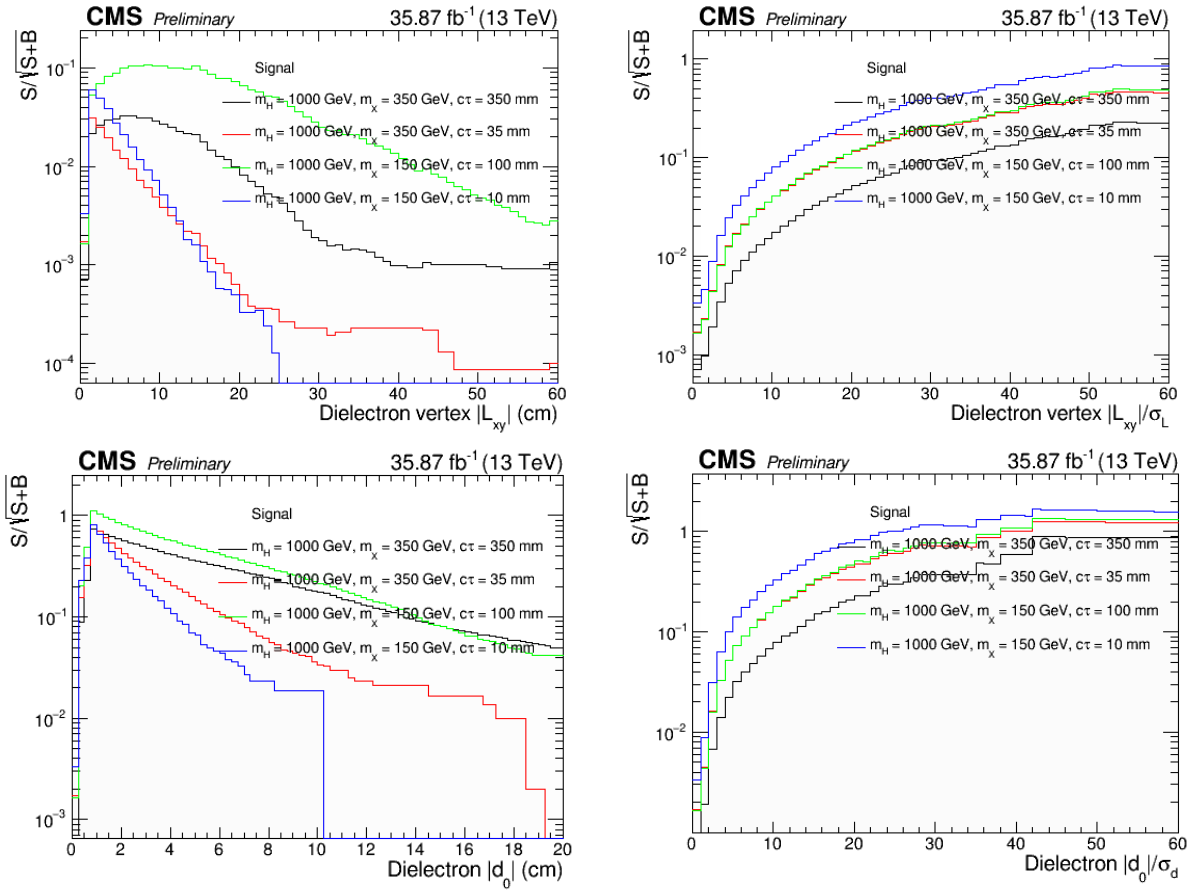

Figure 5.17: Signal significance in electron channel for the case of Higgs boson mass = 1000 GeV. Upper left: L_{xy} , upper right: I_{xy} , lower left: d_{xy} , lower right: $d_{xy}/\sigma(d_{xy})$.

For all variables and all signals considered in figure 5.16, the figure of merit is low and is mostly below 1, this is because the signal is much lower than the background for the high set. Nevertheless, the shape of the signals resembles the case of low Higgs boson mass seen in figure 5.13, but with some particular differences, like how the maximum for the 1000_150_100 signal is more displaced to the right, or how all signals peak more to the right in the I_{xy} case.

In the L_{xy} case, the signal significance tends to be the lowest among all variables shown in figure 5.17, even the 1000_150_100 signal which has the highest figure of merit in all the rank only reaches $FoM \approx 10^{-1}$ at its maximum that happens to be a flat region in the range $5\,cm < L_{xy} < 15\,cm$. Below is the 1000_350_350 signal that has a maximum at $L_{xy} \approx 5\,cm$ then it decreases but in the shown range reaches a flat minimum in the region $L_{xy} > 40\,cm$. The remaining signals, with a lower life-time, decrease more steeply.

As for I_{xy} , the signal significance of the 4 signals all follow a similar shape. In this case the 1000_350_35 signal and the 1000_150_100 are practically overlapped, this is related to how close their reconstruction was as seen in figure 5.15. The figure of merit also increases in the considered range until it reaches a flat region at $I_{xy} \approx 52$, here the 1000_350_350 signal is close to 1 from below.

The figure of merit for d_{xy} is at its highest when $d_{xy} \approx 1\,cm$ for all the signals, with a value in the order of 1. The pair of signals with higher mean life-time remains above the pair with lower mean life-time in all the range.

In the case of $d_{xy}/\sigma(d_{xy})$ we see that its signal significance describes a very similar shape to the I_{xy} case for all signals, even the ordering and the fact that the 1000_350_35 and 1000_150_100 are overlapped is the same. The signal significance increases with $d_{xy}/\sigma(d_{xy})$ until reaching a flat maximum at $d_{xy}/\sigma(d_{xy}) \approx 42$, here this value approaches to 1 from below in the case of the 1000_350_350 signal, and above 1 for the others. For I_{xy} and $d_{xy}/\sigma(d_{xy})$ this figure of merit increases because the signals for these variables are relatively flat in their reconstruction as seen in figure 5.15, whereas the background should be decreasing, this would increase the signal significance according to definition (5.2).

The signal significance was also obtained for the high set in the muon case, the results are shown in the plots of figure 5.18:

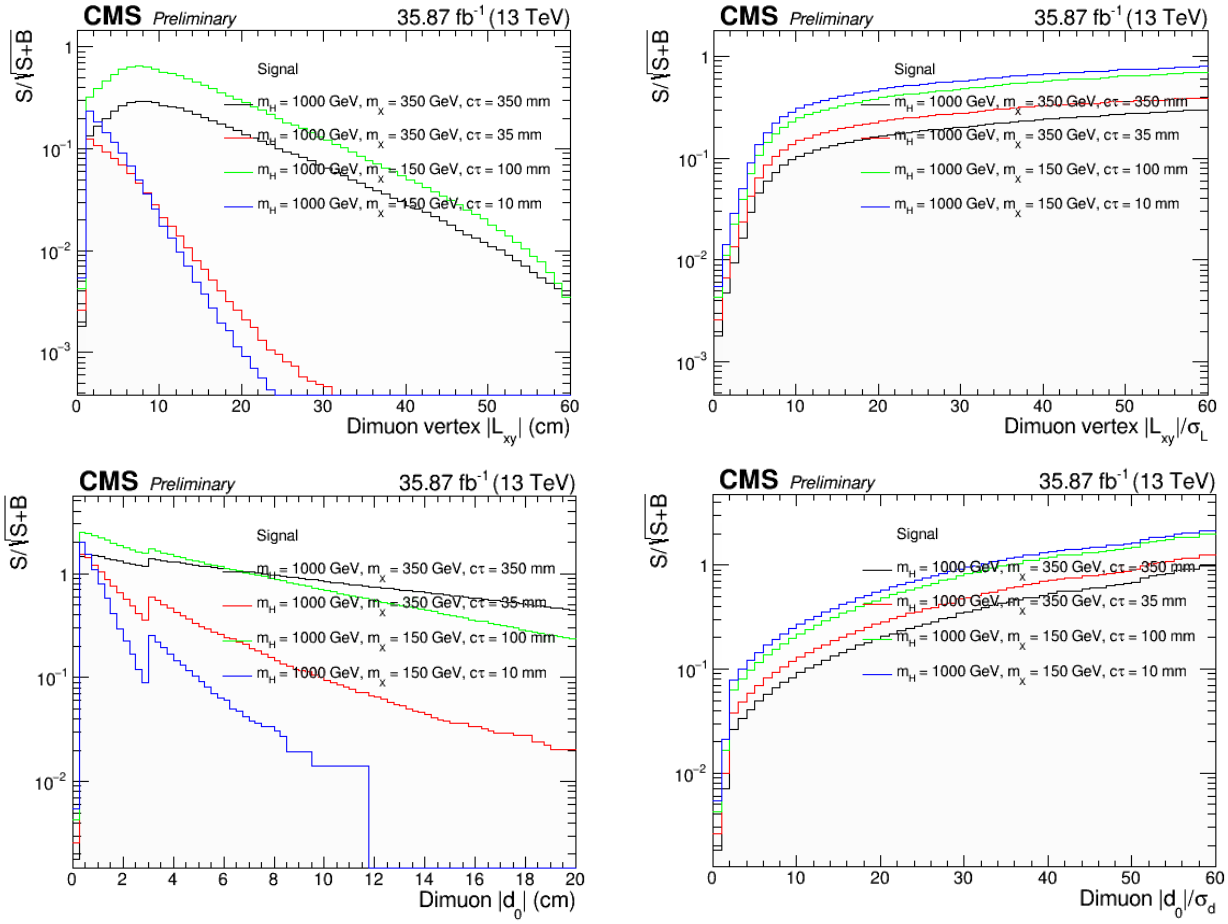

Figure 5.18: Signal significance in muon channel for the case of Higgs boson mass = 1000 GeV. Upper left: L_{xy} , upper right: I_{xy} , lower left: d_{xy} , lower right: $d_{xy}/\sigma(d_{xy})$.

Here we can see similar results to those of the electron case in figure 5.17, but with a tendency to have more signal significance in the case of L_{xy} and d_{xy} , the same that happened with the low set of signals discussed before, this too would be a result of higher efficiency in muon reconstruction.

The signal significance of L_{xy} never goes above 1. Here the 1000_350_350 and 1000_150_10 are the ones to fall more quickly from an early maximum at $L_{xy}=1-2\,cm$. The other pair of signals also resemble each other with a more soft curve and a maximum at $L_{xy}\approx 5-10\,cm$. The 1000_150_100 signal has the highest signal significance through most of the considered range but the very end at $L_{xy}=60\,cm$ where it is overtaken by the 1000_350_350 signal. Here we see a dependency with the mean life-time as expected.

In the case of I_{xy}, the figure of merit shows a similar shape for all signals, with a very steep growth until $I_{xy}\approx 10$, and then a less steep growth onward. This signal significance does not become as flat compared to the low set of signals shown in figure 5.14 in the considered range.

For d_{xy}, the signals peak at the beginning when $d_{xy}=1-2\,cm$ and then fall, we see a small second peak at $d_{xy}\approx 3\,cm$ for all signals, this is because after this point the background is very small or zero, the background suffers sudden fluctuations as it is very small or zero. Here the signals with higher mean life-time tend to have a higher signal significance and go further in d_{xy}. The 1000_150_100 has higher signal significance than the 1000_350_350 in a short interval until $d_{xy}\approx 5\,cm$ but after that, the later overtakes the former. Also, for this variable we see a signal significance that goes above 1 from $d_{xy}\approx 0.25\,cm$ to $d_{xy}\approx 7\,cm$ in the case of the two signals with higher mean life-time and before $d_{xy}\approx 2\,cm$ for the other pair.

The figure of merit for $d_{xy}/\sigma(d_{xy})$ in figure 5.18 shows similarities in shape and in the ordering of signals with the one for I_{xy}. In this case we have a very steep growth until $d_{xy}/\sigma(d_{xy})=2-3$ and a less steep growth onward. For the considered range, the signal significance does not become flat, unlike what was found for the low mass set in figure 5.14.

5.3 Flight distance VS impact parameter

In this section, flight distance and impact parameter are briefly compared at generation level to evaluate preliminary if the usage of the combined information of this kind of variables could improve the analysis in the future. But here the discussion will be limited to directly compare one to the other for the set of signals in table 5.1.

For X bosons, the flight distance vs impact parameter in the case of muon production is presented in 2D histograms, shown in figure 5.19, for different signals with a color gradient representing the number of events.

The upper limit of the impact parameter has a linear-like proportionality with the flight distance, with values distributed forming a triangular shape. As, by definition, d_{xy} cannot take larger values than L_{xy}. We observe that the signals present a different behavior, with the more boosted ones such as 400_50_40 (see figure 5.9) displaying a more elongated shape along the L_{xy} axis. This is due to the fact for such signals the leptons tend to be more collinear with the vector that goes from the primary to the secondary vertex.

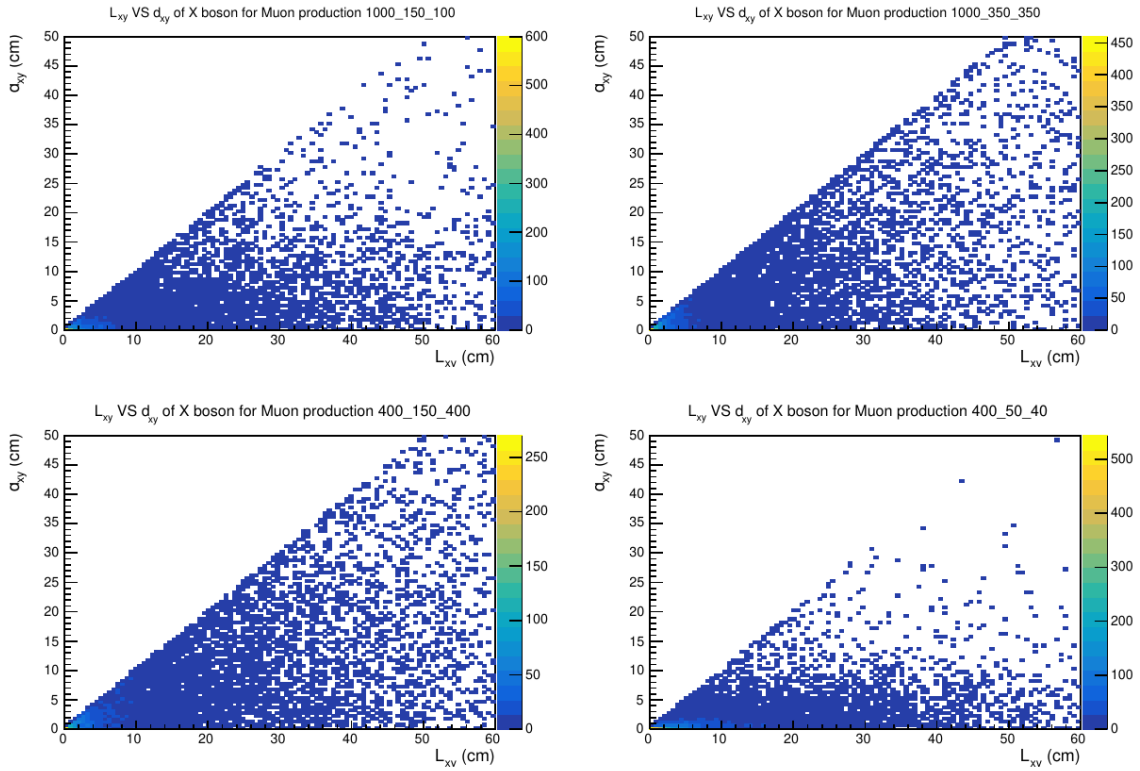

Figure 5.19: Flight distance vs Impact parameter of X boson for muon production.

Here we see for instance that there is a certain region with low values of d_{xy} but sizable values of L_{xy}. This points towards that only using one of those variables could not be the most optimal approach is some cases. However further studies would be needed to decide how to combine the information of both kind of variables.

6. CONCLUSIONS

In this work, a hypothetical process in which a long-lived particle decays into leptons was explored. The analysis was based on an ongoing search for long-lived particles decaying to final states with dileptons at the CMS for proton-proton collisions with a centre of mass energy of 13 TeV. Here a process was considered where a non SM Higgs boson decays into a pair of long-lived X bosons, each of which then decaying into either a dielectron or dimuon.

At generation level, kinematics for the leptons, Higgs boson and X boson where studied for a set of four signals with varying Higgs boson mass, X boson mass and X boson lifetime, also the flight distance of the X boson was explored for each case. Here it was found that the signals had considerably different kinematics, as transverse momentum, energy, pseudorapidity and gamma factor where studied, this could be useful in understanding the differences in efficiency at reconstruction level as well as identifying optimal cuts. The electron and muon decays are considered separately despite the fact that at generator level they show the same behavior, as the differences at reconstruction level are very important. This would facilitate further studies that could rely both on generator and reconstruction level information (like efficiency studies).
Also an algorithm was written to pick a pair of leptons coming from the same displaced vertex and identify its parent X boson particle, this was used to explore the possibility that the angle described by the momentum of the leptons changes depending on the final state α , although no significant difference was found here, this approach could easily be used in a future analysis to look for discrepancies in other variables depending on the final state products. And very importantly for the theme of this work, the flight distance was explored at generation level for the X boson, finding an expected behavior, that is, each signal shows a decreasing exponential-like behavior with the distance; and the lowest the mean lifetime is, the most rapidly it falls.

Then at reconstruction level, four variables were studied: flight distance L_{xy} , flight distance to error ratio I_{xy} , impact parameter d_{xy} and impact parameter to error ratio $d_{xy}/\sigma(d_{xy})$, and to evaluate their performance a figure of merit called signal significance was calculated, which is frequently used in particle physics. Here the scope was extended to eight signals divided in two sets of four signals each depending on the considered Higgs boson mass: the low set for 400 GeV and the high set for 1000 GeV. The reason to do this was due to the considerable differences in the cross sections of the signals. Also, for the first set the signals were comparable to the background in some regions of the variables and in some cases they went above the background, while the later set of signals were well below the background.

Another difference, although less extreme, is that muon reconstruction shows generally higher results in all the four variables and for the both sets, this calculated signal significance also reflects this. An important contribution to this difference would be that electrons are more affected by bremsstrahlung radiation than muons.

It was also observed that the signal significance for the L_{xy} and d_{xy} variables had a decreasing tendency, meanwhile for I_{xy} and $d_{xy}/\sigma(d_{xy})$ this figure of merit increases from the beginning, stabilizing and becoming flat for the low set, while it keeps increasing in the high set, although this could be due to the limited range evaluated in this work. Then the optimal cuts are more stable for the later pair of variables but are not the same for all samples as it tends to be higher for the signals with a Higgs mass of 1000 GeV.
Also for the low set, the flat maximum of the I_{xy} and $d_{xy}/\sigma(d_{xy})$ signal significances are of the same order of magnitude than the sharp early maximum for the L_{xy} and d_{xy} cases. This makes

the I_{xy} and $d_{xy}/\sigma(d_{xy})$ variables interesting in supporting future analysis on LLPs. Given that the cuts on the significance variables are not the same for every signal, a possible approach that could be explored in order to keep the most possible sensitivity to a broad spectrum of signal parameters could be to introduce different signal regions instead of applying only one lower cut to the considered variable.

Finally, L_{xy} and d_{xy} where directly compared at generation level. The resulting plots describe bounded regions for the simulated Monte Carlo events, finding a more elongated shape along the L_{xy} axis for more boosted samples. Then, instead of using only a variable such as L_{xy} or d_{xy} (or the corresponding significances), it could be explored to use the combined information of both variables in a future analysis to see if there are cases where sensitivity is improved with respect to the single variable approach.

REFERENCES

[1] S. F. Novaes. “Standard Model: An introduction”. In: arXiv hep-ph/0001283v1 (2000), p. 17.

[2] Serguei Chatrchyan et al. “Observation of a new boson at a mass of 125 GeV with the CMS experiment at the LHC”. In: Physics Letters B 716.1 (2012).

[3] Georges Aad et al. “Observation of a new particle in the search for the Standard Model Higgs boson with the ATLAS detector at the LHC”. In: Physics Letters B 716.1 (2012).

[4] Celia Fernández Madrazo, Pablo Martínez Ruiz del Árbol, and Jesús Manuel Vizán García. “Search for Long-Lived Particles decaying to final states with a displaced dilepton vertex in proton-proton collisions at √s=13 TeV”. CMS internal document (ongoing).

[5] P.A. Zyla et al. “(Particle Data Group 2020) Particle Physics Booklet”. 2020.

[6] Susanne Mertens. “Direct Neutrino Mass Experiments”. In: arXiv:1605.01579v1 [nucl-ex] (5 May 2016), p. 1.

[7] Peter W. Higgs (1964). "Broken symmetries and the masses of gauge bosons". Physical Review Letters. 13 (1964): 508–09. doi:10.1103/PhysRevLett.13.508.

[8] Samuel J. Ling, Jeff Sanny, William Moebs. “University Physics”. Volume 3. OpenStax, Rice University, 2018, p. 530.

[9] Mark Thomson. “Modern Particle Physics”. Cambridge University Press 2013.

[10] E. Corbelli; P. Salucci. "The extended rotation curve and the dark matter halo of M33". In: Monthly Notices of the Royal Astronomical Society. 311 (2000).

[11] G. Bertone; D. Merritt. "Dark Matter Dynamics and Indirect Detection". In: Modern Physics Letters A. 20 (2005): 1021–1036, pp. 1,2.

[12] Michael Dine. “The Origin of the Matter-Antimatter Asymmetry”. In: arXiv hep-ph/0303065v3 (17 Jun 2003), p. 2.

[13] G. Rajasekaran. “THE STORY OF THE NEUTRINO”.In: arXiv:1606.08715v2 [physics.pop-ph] (14 Oct 2016), p. 16.

[14] Y. Fukuda et al. (Super-Kamiokande Collaboration). In: "Evidence for Oscillation of Atmospheric Neutrinos". Physical Review Letters. 81 (24 August 1998): 1562–1567.

[15] Nathaniel Craig. “Naturalness Hits a Snag with Higgs”. APS Physics 13 (2020) 174. DOI:10.1103/Physics.13.174.

[16] Stephen P. Martin. “A Supersymmetry Primer”. In: arXiv:hep-ph/9709356 (2016), p. 60.

[17] A. Djouadi. “The Minimal Supersymmetric Standard Model: Group Summary Report”. In: arXiv:hep-ph/9901246 (1999).

[18] David Curtin, et al. “Long-lived particles at the energy frontier: the MATHUSLA physics case”. In: Rep. Prog. Phys.82 116201 (2019).

[19] Iva Raynova (18 January, 2018). “Long-lived physics“. Retrieved from: https://home.cern/news/news/experiments/long-lived-physics.

[20] M. Aaboud et al. “Search for long-lived particles produced in pp collisions at √s=13 TeV that decay into displaced hadronic jets in the ATLAS muon spectrometer”. In: Phys. Rev. D 99, 052005 (2019), p. 3.

[21] Lawrence Lee, Christian Ohm, Abner Soffer, Tien-Tien Yu. “Collider Searches for Long-Lived Particles Beyond the Standard Model”. JPPNP 3695 (2019), p. 5.

[22] “The Large Hadron Collider”. CERN. Retrieved from: https://home.cern/science/accelerators/large-hadron-collider on may 28, 2021.

[23] Chris Llewellyn Smith. “Genesis of the Large Hadron Collider”. In: Philosophical Transactions A. 373: 20140037 (2015).

[24] Jorg Wenninger. “The LHC collider”. In: Comptes Rendus Physique Volume 16, Issue 4 (May 2015).

[25] “Facts and figures about the LHC”. CERN. Retrieved from: https://home.cern/resources/faqs/facts-and-figures-about-lhc on may 31, 2021.
[26] A. Maevskaya. “ALICE FIT data processing and performance during LHC Run 3”. In: arXiv:2012.02760 [physics.ins-det] (2020), p. 2.
[27] J. T. Boyd. “LHC Run-2 and Future Prospects”. In: arXiv:2001.04370 [hep-ex] (2020).
[28] Cecilia E. Gerber. “LHC Highlights and Prospects”. In: arXiv:1909.10919 [hep-ex] (2019), p. 1.
[29] “CMS”. CERN. Retrieved from: https://home.cern/science/experiments/cms on june 1, 2021.
[30] “About CMS”. CERN. Retrieved from: https://cms.cern/detector on june 1, 2021.
[31] A. M. Sirunyan et al. “Particle-flow reconstruction and global event description with the CMS detector”. In: JINST 12 (2017) P10003. DOI: 10.1088/1748-0221/12/10/P10003.
[32] V. Khachatryan et al. The CMS Collaboration. “CMS Tracking Performance Results from Early LHC Operation”. In: Eur.Phys.J.C70:1165-1192 (2010).
[33] S. Chatrchyan et al. The CMS Collaboration. “Description and performance of track and primary-vertexreconstruction with the CMS tracker”. In: JINST 9 (2014) P10009.
[34] “Silicon Strips”. CERN. Retrieved from: https://cms.cern/detector/identifying-tracks/silicon-strips on june 16, 2021.
[35] L. Viliani. “CMS tracker performance and readiness for LHC Run II”. In: Nuclear Instruments and Methods in Physics Research A 824 (2016).
[36] Sirunyan et al. The CMS Collaboration. “Precision measurement of the structure of the CMS inner tracking system using nuclear interactions”. In: JINST 13 (2018) P10034.
[37] N. Parashar. “CMS Pixel Detector Upgrade”. In: arXiv:1110.2125 [physics.ins-det] (2011).
[38] CMS Collaboration. “The Phase-2 Upgrade of the CMS Tracker, Technical Design Report”. In: CERN-LHCC-2017-009, CMS-TDR-014 (2017).
[39] Federico Ferri. “The CMS ECAL Phase-2 upgrade for high precision energy and timing measurements”. In: Nuclear Instruments and Methods in Physics Research Section A: Accelerators, Spectrometers, Detectors and Associated Equipment Volume 958, 162159 (2020).
[40] “Energy of Electrons and Photons (ECAL)”. CERN. Retrieved from: https://cms.cern/detector/measuring-energy/energy-electrons-and-photons-ecal on june 23, 2021.
[41] Cristina Biino. “The CMS Electromagnetic Calorimeter: overview, lessons learned during Run 1 and future projections”. In: Journal of Physics: Conference Series587 (2015) 012001. DOI: 10.1088/1742-6596/587/1/012001.
[42] P. Vichoudis, D. Barney, R. Berberat, D. Di Calafiori, O. Holme, A. Honma, S. Kaufmann, E. Magnin, P. Petit, P.P. Trapanic, S. Zelepukinb. “The upgraded CMS Preshower high voltage system”. In: JINST 8 C01050 (2013).
[43] Abraham Tishelman-Charny. “Optimizing the Performance of the CMS ECAL Trigger for Runs 2 and 3 of the CERN LHC”. In: arXiv:1910.06232 [physics.ins-det] (2019).
[44] S. Chatrchyan et al. The CMS Collaboration. “Performance of the CMS Hadron Calorimeter with Cosmic Ray Muons and LHC Beam Data”. In: arXiv:0911.4991 [physics.ins-det] (2010).
[45] G.L. Bayatian, et al. The CMS Collaboration. “The Hadron CalorimeterTechnical Design Report”. In: CERN/LHCC 97-31, CMS TDR 2 (1997).
[46] A.M. Sirunyan, et al. The CMS Collaboration. “Calibration of the CMS hadron calorimeters using proton-proton collision data at √s=13 TeV”. In: arXiv:1910.00079v2 [physics.ins-det] (2020).

[47] “Energy of Hadrons (HCAL)”. CERN. Retrieved from: https://cms.cern/detector/measuring-energy/energy-hadrons-hcal on june 24, 2021.
[48] B. S. Acharya, et al. “The CMS Outer Hadron Calorimeter”. In: CMS-NOTE-2006/127 (2006).
[49] F. Kircher, et al. “Status Report on the CMSSuperconducting Solenoid for LHC”. In: IEEE Transactions on Applied Superconductivity, Volume 9, Issue 2 (June 1999).
[50] F. Kircher, et al. “Final Design of the CMS Solenoid Cold Mass”. In: IEEE Transactions on Applied Superconductivity, Volume 10, Issue 1 (March 2000) .
[51] Cesare Calabria. “Measurement and simulation of the background in the CMS muon detectors”. In: EPJ Web of Conferences 214, 02020 (2019).
[52] S. Chatrchyan, et al. The CMS Collaboration. “The performance of the CMS muon detector in proton–proton collisions at √s=7 TeV at the LHC”. In: JINST 8 (2013) P11002.
[53] A.M. Sirunyan ,et al. The CMS Collaboration. “Performance of the CMS muon detector and muon reconstruction with proton-proton collisions at √s=13 TeV”. In: arXiv:1804.04528 [physics.ins-det] (2018).
[54] S. Chatrchyan, et al. The CMS Collaboration. “The CMS experiment at the CERN LHC”. In: Journal of Instrumentation 3 S08004 (2008).
[55] P. Giacomelli. “The CMS muon detector”. In: Nuclear Instruments and Methods in Physics Research A 478 (2002) 147–152.
[56] C. Foudas. “The CMS Level-1 Trigger at LHC and Super-LHC”. In: arXiv:0810.4133 [physics.ins-det] (2008).
[57] W. Adam, et al. The CMS Trigger and Data Acquisition Group. “The CMS High Level Trigger”. In: Eur.Phys.J.C46:605-667 (2006). DOI: 10.1140/epjc/s2006-02495-8.
[58] G Petrucciani et al. “Mini-AOD: A New Analysis Data Format for CMS”. In: J. Phys.: Conf. Ser.664 072052 (2015).
[59] “The Grid: A system of tiers”. CERN. Retrieved from: https://home.cern/science/computing/grid-system-tiers on june 3, 2021.
[60] D. Bonacorsi, the CMS Collaboration. “The CMS Computing Model”. In: Nuclear Physics B - Proceedings Supplements Volume 172 (October 2007) pp. 53-56.
[61] CMS Collaboration. “CMS The Computing Project, Technical Design Report”. In: CERN/LHCC 2005-023, CMS TDR 7 (2005).
[62] A.M. Sirunyan et al. The CMS Collaboration. “Electron and photon reconstruction and identification withthe CMS experiment at the CERN LHC”. In: JINST 16 (2021) P05014.
[63] “Finding electrons and photons with the CMS detector”. CERN. Retrieved from: https://cms.cern/news/finding-electrons-and-photons-cms-detector on june 5, 2021.
[64] CMS Collaboration. “Search for long-lived particles decaying to final states that include dileptons”. In: Phys. Rev. D 91 (2015) 052012. DOI: 10.1103/PhysRevD.91.052012.
[65] N. Neumeister. “Muon Reconstruction Software in CMS”. In: Computing in High Energy Physics and Nuclear Physics (2004), pp.384
[66] CMS Collaboration. “Muon Reconstruction and Identification Improvements for Run-2 and First Results with 2015 Run Data”. In: CMS Detector Performance Summaries CMS-DP-15-015 (2015).
[67] CMS Collaboration. “Measurement of Momentum Scale and Resolution of the CMS Detector using Low-mass Resonances and Cosmic Ray Muons”. In: CMS PAS TRK-10-004 (2010).
[68] S. Chatrchyan, at al. The CMS Collaboration. “Description and performance of track and primary vertex reconstruction with the CMS tracker”. In: JINST 9 (2014) P10009. DOI: 10.1088/1748-0221/9/10/P10009.
[69] Wolfgang Adam. “Track and vertex reconstruction in CMS”. In: Nuclear Instruments and Methods in Physics Research A 582 (2007) 781–784.

[70] D. Miller, D.R. Tovey, J.D. Jackson, Particle Data Group. “Kinematics”. In: Particle Data Group Reviews (2019).
[71] Laura Trujillo Taborda. “Search for Long Lived Particles at the LHC”. In: Masters Thesis, IFCA (2020).
[72] CMS Collaboration. “CMS Physics Analysis Summary”. In: CMS PAS BTV-07-002 (2009).
[73] Ilya Narsky. “Optimization of Signal Significance by Bagging Decision Trees”. In: arXiv:physics/0507157 [physics.data-an] (2005).

ANNEXES

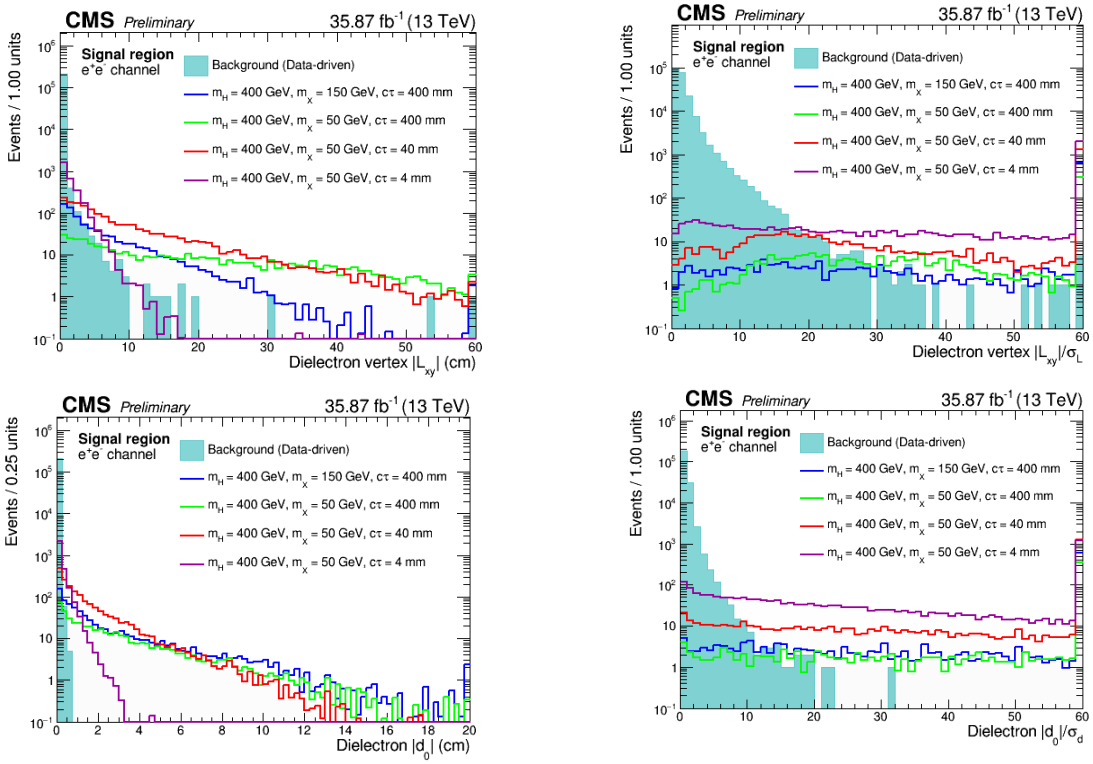

Figure A.1: Off-Z reconstruction in electron channel for the case of Higgs boson mass = 400 GeV. Upper left: L_{xy} , upper right: I_{xy} , lower left: d_{xy} , lower right: $d_{xy}/\sigma(d_{xy})$.

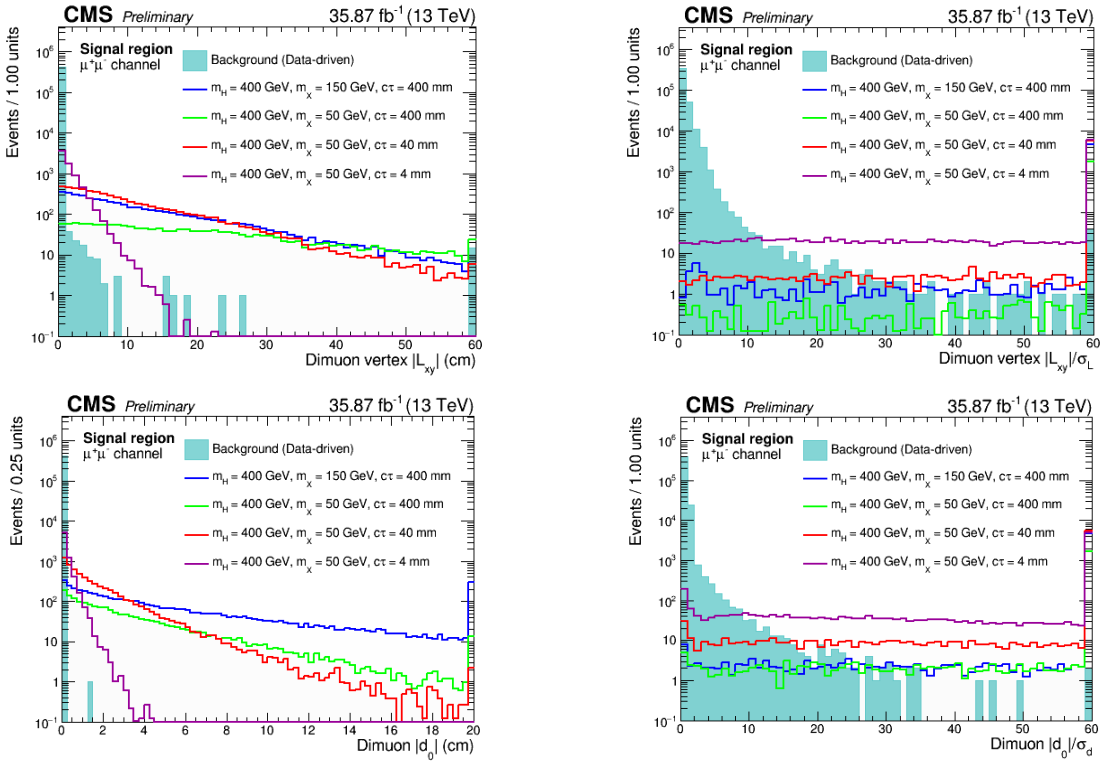

Figure A.2: Off-Z reconstruction in muon channel for the case of Higgs boson mass = 400 GeV. Upper left: L_{xy} , upper right: I_{xy} , lower left: d_{xy} , lower right: $d_{xy}/\sigma(d_{xy})$.

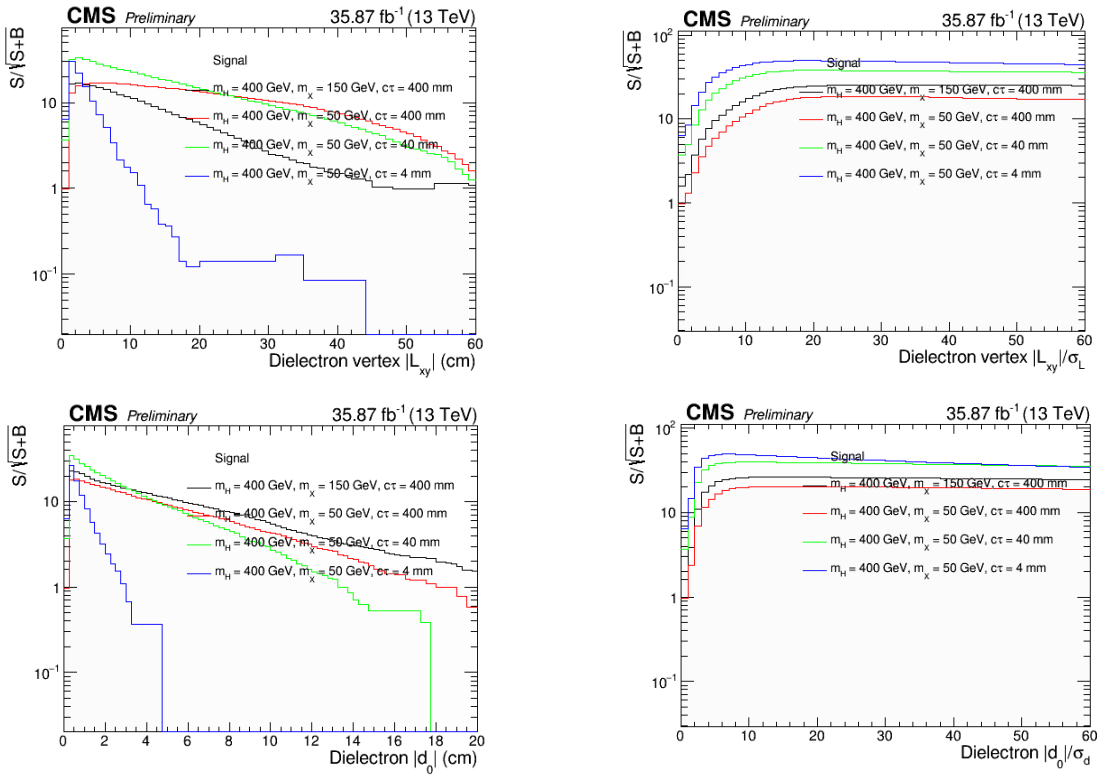

Figure A.3: Off-Z Signal significance in electron channel for the case of Higgs boson mass = 400 GeV. Upper left: L_{xy} , upper right: I_{xy} , lower left: d_{xy} , lower right: $d_{xy}/\sigma(d_{xy})$.

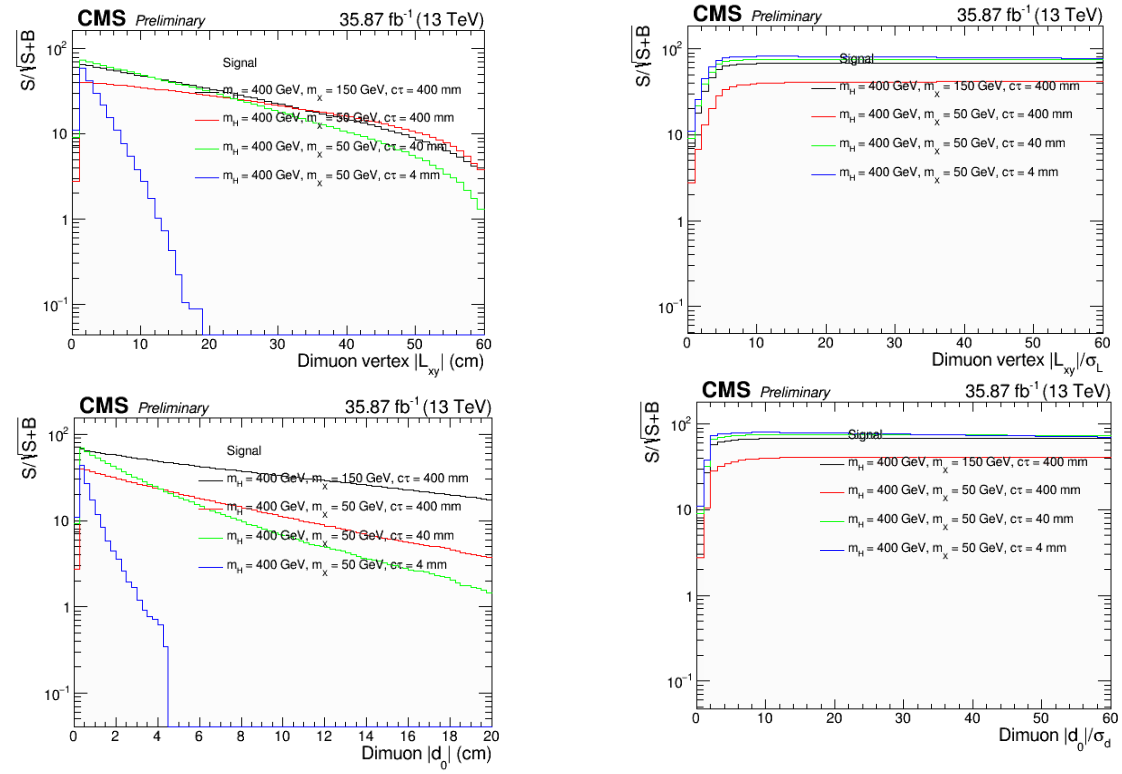

Figure A.4: Off-Z Signal significance in muon channel for the case of Higgs boson mass = 400 GeV. Upper left: L_{xy} , upper right: I_{xy} , lower left: d_{xy} , lower right: $d_{xy}/\sigma(d_{xy})$.